Understanding monsoon controls on the energy and mass balance of ~~Himalayan~~ glaciers in the Central and Eastern Himalaya

Authors: Stefan Fugger[1,2], Catriona L. Fyffe[1,3], Simone Fatichi[4], Evan Miles[1], Michael McCarthy[1,5], Thomas E. Shaw[1], Baohong Ding[6], Wei Yang[6], Patrick Wagnon[7], Walter Immerzeel[8], Qiao Liu[9], and Francesca Pellicciotti[1,3]

[1]Swiss Federal Institute for Forest, Snow and Landscape Research (WSL),Birmensdorf, Switzerland
[2]Institute of Environmental Engineering, ETH Zurich, 8093 Zurich, Switzerland
[3]Department of Geography and Environmental Sciences, Northumbria University, Newcastle, UK
[4]Department of Civil and Environmental Engineering, National University of Singapore, Singapore
[5]British Antarctic Survey, Cambridge, UK
[6]Institute of Tibetan Plateau Research, Chinese Academy of Sciences, Beijing, China
[7]Univ. Grenoble Alpes, CNRS, IRD, Grenoble-INP, IGE, 38000 Grenoble, France
[8]Faculty of Geosciences, Department of Physical Geography, Utrecht University, Utrecht, The Netherlands
[9]Institute of Mountain Hazards and Environment, Chinese Academy of Sciences, Chengdu, China

Correspondence: Stefan Fugger (stefan.fugger@wsl.ch)

Abstract. The Indian and East Asian Summer Monsoons shape the melt and accumulation patterns of glaciers in High Mountain Asia in complex ways due to the interaction of persistent cloud cover, large temperature ~~amplitudes~~ranges, high atmospheric water content and high precipitation rates. ~~While the monsoons dominate the climate of the southern and eastern regions, they progressively lose strength westward towards the Karakoram, where the influence of Westerlies is predominant.~~ ~~Despite the major role of the monsoon in the Himalayas, a holistic understanding of their influence on the region's glaciers is lacking because previous applications of energy- and mass-balance models have been limited to single study sites~~Glacier energy and mass balance modelling using in-situ measurements offer insights into the ways in which surface processes are shaped by climatic regimes. In this study, we use a full energy- and mass-balance model and seven on-glacier automatic weather station datasets from different parts of the ~~Himalayas~~ Central and Eastern Himalaya to investigate how monsoon conditions influence the glacier surface energy and mass balance. In particular, we look at how debris-covered and debris-free glaciers respond differently to monsoonal conditions. The radiation budget ~~mostly~~ primarily controls the melt of clean-ice glaciers, but turbulent fluxes ~~also~~ play an important role in modulating the melt energy on debris-covered glaciers. The sensible heat flux ~~reduces~~ decreases during core monsoon, but the latent heat flux ~~removes energy from~~ cools the surface due to evaporation of liquid water. This interplay of radiative and turbulent fluxes ~~, together with compensations between increasing and decreasing melt rates over the diurnal cycle,~~ causes debris-covered glacier melt rates to stay almost constant ~~over the entire ablation period~~ through the different phases of the monsoon. Ice melt under thin debris, on the other hand, is amplified by both the dark surface ~~albedo~~ and the turbulent fluxes, which ~~act as a source of energy~~ intensify melt during monsoon through surface heating and condensation~~, especially during monsoon~~. Pre-monsoon snow cover can considerably delay melt onset and have a strong impact on the seasonal mass balance. Intermittent monsoon snow cover ~~further modulates~~ lowers the melt rates at high elevation. ~~Given~~

1

20 ~~our~~ Based on these results, we expect the mass balance of thick debris-covered glaciers to react less sensitively to projected future monsoon conditions than clean-ice and ~~dirty-ice glaciers~~ glaciers with very thin debris. This work is fundamental to the understanding of the present and future Himalayan cryosphere and water budget~~evolution~~, while informing and motivating further glacier- and catchment-scale research using process-based models.

~~(Yang et al., 2017)~~

1 Introduction

25

High Mountain Asia (HMA) holds the largest ice volume outside the polar regions (Farinotti et al., 2019) and due to the large elevation range and vast geographic extent, HMA glaciers are highly diverse in character and hydro-climatic ~~situation~~ context (Yao et al., 2012). Several large-scale weather patterns interact with the region's topography (Bookhagen and Burbank, 2010), causing glaciers~~to '~~ contrast in terms of hypsometry (Scherler et al., 2011a) and accumulation and ablation season-
30 ality (Maussion et al., 2014). The Indian Summer Monsoon dominates the Central Himalaya and the Southeastern Tibetan Plateau during summer, and gradually loses strength moving towards the Karakoram, Pamir and Kunlun ranges in the ~~east~~west, where the influence of Westerlies is particularly strong. A more continental ~~, monsoon-westerlies-influenced regime~~regime, influenced by both monsoon and westerlies, controls the Central Tibetan Plateau (Yao et al., 2012; Mölg et al., 2014), ~~and while~~ the East Asia Monsoon influences the eastern slopes of the Tibetan Plateau ~~(Maussion et al., 2014; Yao et al., 2012)~~
35 (Yao et al., 2012; Maussion et al., 2014). These major modes of atmospheric circulation ~~do not only~~ control the surface processes and runoff regimes of glaciers ~~(e.g. Mölg et al., 2014, 2012; Kaser et al., 2010) but also~~ (e.g. Kaser et al., 2010; Mölg et al., 2012, 20 and lead to distinct responses of glaciers to climate change ~~(Yao et al., 2012; Sakai and Fujita, 2017; Scherler et al., 2011b; Kraaijenbrink e . For example, mass~~ (Scherler et al., 2011b; Yao et al., 2012; Sakai and Fujita, 2017; Kraaijenbrink et al., 2017). Mass losses are high throughout most of HMA, and are particularly pronounced on the South-Eastern Tibetan Plateau, while glaciers exhibit
40 a ~~near-balance regime in~~ near-neutral mass balance regime throughout the Karakoram, Pamir and Kun Lun ~~(Farinotti et al., 2020; Gardelle e~~ (Gardelle et al., 2012; Brun et al., 2017; Farinotti et al., 2020; Shean et al., 2020).

Accurate glacier mass balance modelling is essential to assess glacier meltwater contribution to mountain water resources, and to predict future glacier states and catchment runoff. Physically-based models of glacier ~~energy-~~ energy and mass balance represent surface and ~~sub-surface~~ subsurface energy fluxes using physical equations to calculate the energy ~~residual, i.e.~~
45 ~~the energy~~ available for melt, and the glacier runoff. ~~They have provided an understanding about the individual processes controlling the glacier mass balance and the climatic sensitivity of glaciers in their specific hydro-climatic environment (e.g. Mölg et al., 2012).~~ Summer-accumulation ~~type~~ glaciers in HMA experience simultaneous accumulation and ablation~~and their mass balances are known to be~~ . Using an energy balance model, Fujita and Ageta (2000) found that the mass balances of this type of glaciers is highly sensitive to climatic variability during the monsoon season~~(Fujita and Ageta, 2000)~~, when warm
50 air temperatures and high ~~moisture influx~~ precipitation rates coincide. Using energy balance modelling for an ~~inter-annual study for~~ interannual study at the Central Tibetan Zhadang glacier, Mölg et al. (2012) demonstrated that the timing of monsoon onset and the associated albedo variability can change ~~melt-rates substantially~~ melt rates considerably in subsequent years. At the

same time, they observed a ~~de-coupling~~ decoupling of the glacier mass balance from the Indian Summer Monsoon ~~'s control during the core~~ during the main monsoon season. Mölg et al. (2014) explain the mass balance variability of Zhadang Glacier

55 as being controlled by both the Indian Summer Monsoon onset and ~~remotely controlled by~~ mid-latitude Westerlies. Combining energy balance with weather forecast modelling, Bonekamp et al. (2019) identify the timing and quantity of snowfalls as the main source of differences in ~~mass-balance~~ mass balance regimes between the Shimshal Valley in the Karakoram and the Langtang Valley in the Central Himalaya. Similarly, Zhu et al. (2018) attribute mass balance differences of three glaciers on the Tibetan Plateau mainly to different local ~~rain-~~rain/~~snowfall~~ snow precipitation ratios and timing.

60   The presence of debris cover, a widespread characteristic of HMA glaciers, ~~(e.g. Herreid and Pellicciotti, 2020; Kraaijenbrink et al., 2017~~ (e.g. Scherler et al., 2011b; Kraaijenbrink et al., 2017; Herreid and Pellicciotti, 2020), creates additional complexity to understanding and modelling the processes leading to (sub-debris) glacier melt. In recent years, much effort has gone into developing energy balance models for debris-covered glaciers, ~~(e.g. Fujita et al., 2014; Reid and Brock, 2010; Nicholson and Benn, 2006; Lejeune et al.~~ . ~~Yang et al. (2017) compares~~ (e.g. Nicholson and Benn, 2006; Reid and Brock, 2010; Lejeune et al., 2013; Fujita et al., 2014; Collier et al.

65 . Yang et al. (2017) compare the energy balance of a debris-covered and a clean-ice glacier on the Southeastern Tibetan Plateau and finds the main differences, beside the differences in melt rates, is their climatic sensitivity and the important role of turbulent fluxes on debris-covered glaciers. ~~Thick~~ Studies with observational data on two Indian glaciers showed that thick debris is a ~~stronger~~ more important control on melt rates than elevation ~~(Shah et al., 2019)~~ (?Shah et al., 2019) and also dampens and delays glacier melt in the diurnal cycle (Shrestha et al., 2020)~~, while melt enhancement can occur where there is very thin~~

70 ~~or patchy debris (Fyffe et al., 2020)~~. Ablation is often expected to be higher on ~~such 'dirty ice glaciers '~~ glaciers with debris around or below the critical thickness (site dependent, 1-5cm) (?) than at both clean-ice sites and at sites with ~~established~~ thicker debris cover, as shown experimentally ~~(Reznichenko et al., 2010; Östrem, 1959)~~(Östrem, 1959; Reznichenko et al., 2010), and by means of modelling ~~(Reid and Brock, 2010)~~(e.g. ?Reid and Brock, 2010), with humidity being a determining factor for this enhancement (Evatt et al., 2015). Moisture in debris is an important factor under monsoonal conditions, controlling the debris'

75 thermal properties and thus ablation (Sakai et al., 2004; Nicholson and Benn, 2006) and has been the focus of devoted modelling studies ~~(Giese et al., 2020; Collier et al., 2014)~~(Collier et al., 2014; Giese et al., 2020). Moreover, the representation of latent heat due to evaporation ~~(Giese et al., 2020; Steiner et al., 2018)~~ (Steiner et al., 2018; Giese et al., 2020) and atmospheric stability correction for turbulent fluxes were shown to be important to improve the simulation of sub-debris melt (Reid and Brock, 2010; Mölg et al., 2012). ~~Model implementation, however, remains complex and difficult to validate and transfer. Nevertheless,~~

80 ~~Nicholson and Stiperski (2020) showed that the turbulent conditions over debris-covered and clean-ice sites are similar enough to be numerically treated in similar ways, i.e. the Monin-Obukhov similarity theory can be leveraged in the same way for the calculation of the turbulent fluxes, but with different parameters.~~Observations of glacier surface meteorology, a prerequisite for accurate energy balance modelling, exist only for a few glaciers in HMA, and even fewer records exist for debris-covered glaciers. Direct observations of glacier mass balance in HMA also remain sparse, and remote sensing observations are hindered~~

85 ~~by heavy cloud cover during the monsoon season.~~Previous studies explicitly dealing with the imprint of the monsoon on the surface thermal properties of glaciers remained limited to individual clean-ice glaciers in the Central Tibetan Plateau (Mölg et al., 2012, 2014).

Our main goal is to improve the understanding of monsoon controls on glaciers ~~in the Himalayan region by leveraging available~~ of various surface types in the Central and Eastern Himalaya. Applying the glacier energy and mass balance module of a land surface model suited to both debris-covered and clean-ice glaciers, and leveraging seven on-glacier automatic weather station (AWS) records ~~in the region. Our specific objectives are~~ from the region, we answer the following questions: 1) ~~to understand, in detail, the glacier~~ Which energy and mass ~~balance and related controls at seven Himalayan study sites in a robust and systematic manner;~~ fluxes dominate the seasonal mass balance of Himalayan glaciers? 2) ~~to assess the effects of monsoonal conditions on debris-covered and clean ice glaciers;~~ How does debris cover modulate the energy balance in comparison to clean-ice surfaces? 3) ~~to investigate whether these effects are generalisable; and 4) to discuss possible implications of our findings under climate change . We address these objectives by applying the glacier energy and mass balance module of a land surface model suited to both debris-covered and clean-ice glaciers~~ How does the monsoon change the glacier surface energy balance? Answering these questions allows us to infer how these glaciers will respond to the possible future changes of the monsoons in the region. We apply the model at the point scale of individual AWSs, driven by high-quality in situ meteorological observations that guarantee accurate energy balance simulations, not affected by extrapolation of the meteorological forcing. By identifying ~~and discussing~~ the key surface processes of glaciers and their dynamics under monsoonal conditions, this study promotes their appropriate representation in models of glacier mass balance and the hydrology of glacierised catchments.

2 Study sites and data

2.1 ~~Sites and observations~~

In situ observations from seven on-glacier ~~automatic weather stations~~ AWSs in different environments along the climatic gradient of the ~~Himalayas~~ Himalaya were gathered and are used for forcing and evaluation of the model (Figure 1 and Table 1). Our seven study sites are located in the Central and Eastern ~~Himalayas~~ Himalaya and cover a range of glacier types and local climates (Figure 1, 2 and Table 2). The seven sites include both spring- (24K, Parlung No.4) and summer-accumulation glaciers (all others) as indicated by the proportion of monsoon precipitation to the annual precipitation (Figure ~~??~~ A1). Langtang, Lirung and Yala are ~~neighboring~~ neighbouring glaciers found in the Langtang Valley (Figure 1)~~, which has an extensive history of glaciological and hydrological reasearch~~. The Langtang Valley is strongly influenced by the Indian Summer Monsoon ($\sim$ June to October), during which more than 70% of the annual precipitation ~~arrives (Figure ??~~ falls (Figure A1 and Table 2), while the period from November to May is a drier season ~~(Collier and Immerzeel, 2015; Immerzeel et al., 2012). The Langtang~~ (Immerzeel et al., 2012; Collier and Immerzeel, 2015). The Valley has been a site of extensive glaciological (e.g. Fujita et al., 1998; Stumm et al., 2020), meteorological ~~(Immerzeel et al., 2014; Heynen et al., 2016; Steiner and Pellicciotti, 2016; Bonekamp et al., 20~~ (Immerzeel et al., 2014; Collier and Immerzeel, 2015; Heynen et al., 2016; Steiner and Pellicciotti, 2016; Bonekamp et al., 2019) and hydrological (e.g. Ragettli et al., 2015) investigations. On-glacier AWSs were installed during the ablation season on Lirung (2012-2015) and Langtang (2019) glaciers, and year-round on Yala (2012-ongoing) (Table 1). Both Lirung and Langtang are valley glaciers that have heavily debris-covered tongues, but the tongue of Lirung has disconnected from the accumulation zone

(Figure 2). Yala is a considerably smaller clean-ice glacier, with most of its ice mass located at comparably high elevation. It is oriented to the southwest and has a gentle slope (Fujita et al., 1998) (Figure 2 and Table 2).

North Changri Nup Glacier (hereafter Changri Nup Glacier) is a debris-covered valley glacier located in the Everest region in Nepal (Figure 1). The southeast-oriented, avalanche-fed glacier discharges into the Koshi River system. The local climate is similar to ~~the one~~ that of the Langtang Valley, with 70-80% of precipitation falling during monsoon (Vincent et al., 2016) (Figure 2, ~~??~~A1 and Table 2).

24K and Parlung No.4 glaciers are located on the southeastern Tibetan Plateau, feeding water into the upper Parlung Tsangpo, a major tributary to the Yarlung Tsangpo - Brahmaputra River. The summer climate is characterized by monsoonal air masses reaching the Gangrigabu mountain range from the south through the Yarlung Tsangpo Grand Canyon. 24K Glacier is an avalanche fed valley glacier with a debris-covered tongue, located 24 km from the town of Bome (Yang et al., 2017). It is small in size, oriented to the northwest and surrounded by shrubland (Figure 1, 2 and Table 2). Parlung No.4 is a debris-free valley glacier, which is north-east oriented, considerably larger than 24K and located 130km ~~(to the~~ south-east ~~)~~ from Bome (Yang et al., 2011) (Figure 1 and Table 2). Full automatic weather stations were installed in the ablation zones of both glaciers in 2016 and subsequent years (Table 1).

Hailuogou Glacier, the second-largest of our study sites (Figure 2) is located on the eastern slope of Mt. Gongga in the easternmost portion of the southeastern Tibetan Plateau (Figure 1). It is located at low elevation and ~~covered with thin and patchy debris~~large parts of its ablation zone are continuously covered with a thin layer of fine clasts and scattered with coarser clasts, leading to high annual ablation rates (Figure 2 and Table 2). The local climate influenced by the East Asia Monsoon with typically only 50 to 60% of the annual precipitation arriving during the monsoon period (Figure 1 and ~~??~~A1). The debris-covered tongue is connected to a steep and extensive accumulation zone via a large icefall, but avalanching is the primary mass supply mechanism through the icefall to the valley tongue (Liao et al., 2020), and a dynamic disconnect is expected to occur in the near future. Weather stations were installed at three nearby off-glacier locations and one on-glacier site during 2008, while precipitation was measured at the Alpine Ecosystem Observation and Experiment Station of Mt. Gongga, within $1.5\,km$ from the glacier terminus (Table 1).

2.1 ~~Climatic and meteorological conditions~~

~~Here, we~~ We use the monthly averaged ERA5-Land reanalysis data (Muñoz Sabater, 2019) to ~~provide an overview of the long term climatic patterns, e.g. the average monsoonal regime from June through September, and~~ evaluate the representativeness of the AWS records in terms of seasonal variability (Figures A3 to A9), ~~while acknowledging that the absolute values from the reanalysis dataset might be biased and do not necessarily represent the conditions at the glacier location.~~and to provide an overview of the long term climatic patterns, e.g. the average monsoonal regime from June through September (Figure A1). We thereby focus on the qualitative aspects, given that the absolute values from the reanalysis dataset are not representative for the AWS location at the glacier surfaces. A detailed description is given in the Supplementary.

~~Incoming shortwave radiation (Figure ??b) shows a clear peak before monsoon onset at all sites. A smaller secondary peak is~~
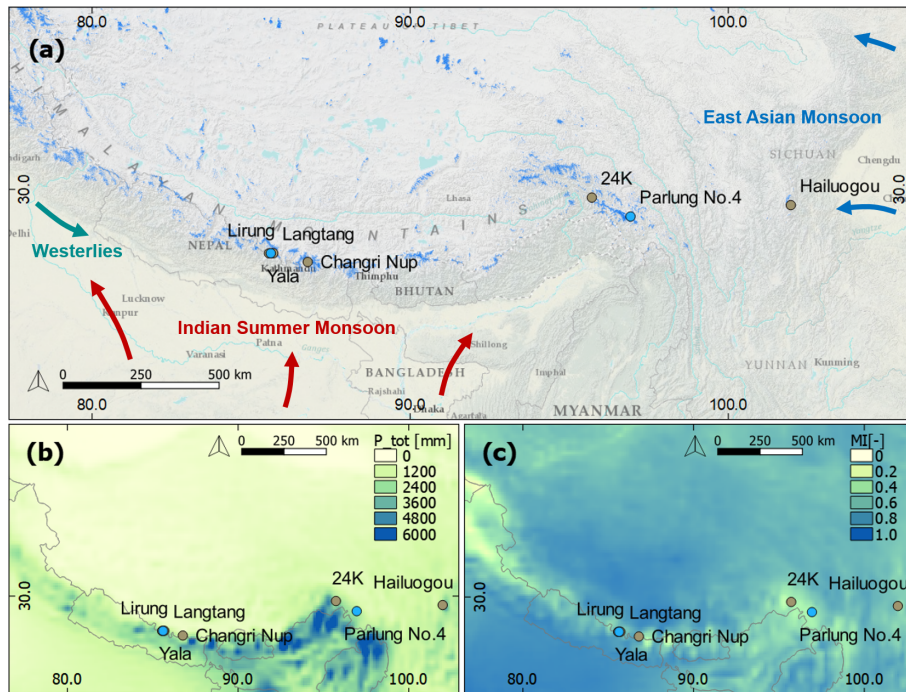
Figure 1. (a) shows the context of study sites with respect to large-scale weather patterns, topography and glacier distribution (~~turqoise~~blue, source: Randolph Glacier Inventory 6.0). Blue dots indicate clean-ice study glaciers and brown dots indicate debris-covered study glaciers. **(b)** displays the spatial pattern of average annual precipitation from ERA5-Land (1981-2019). **(c)** shows the monsoonal (June-September) portion of the ERA5-Land total annual precipitation (MI). Background map source: ESRI, U.S. National Park Service.

155 ~~reached just after the monsoon in October at the Central Himalayan sites, but not at the Eastern Himalayan sites. Interruptions in monsoonal overcast conditions (break periods) seem to be more common at the eastern sites, leading to occasional secondary peaks in incoming shortwave radiation during monsoon.Average mean monthly 2 m air temperatures have a similar pattern at all study sites (Figure ??a), with a slow increase from January to a peak between July and August, just after peak monsoon, and a steeper decline from post-monsoon into winter. A similar regime is followed by $LW_\downarrow$, with highest values reached~~

160 ~~during the core monsoon (Figure ??c).There is a clear difference in the seasonal evolution of precipitation between the Central (Lirung, Lantang, Yala, Changri Nup) and the Eastern Himalayan sites (24K, Parlung No.4, Hailuogou) (Figure ??e): relatively high mean monthly precipitation during the monsoon period is contrasted by comparably low precipitation outside of this period.The eastern sites have less pronounced monsoonal precipitation peaks, and more gradual changes in precipitation intensities over the annual cycle. The Parlung sites (24K and Parlung No.4) have two precipitation peaks: during spring and~~

165 ~~monsoon. Hailuogou exhibits the smoothest evolution over the annual cycle with a clear maximum in July. A simple monsoon index (MI) is calculated for each year including the study year as the ratio between monsoon precipitation and annual average precipitation (Figure ??e). This value tends to be higher in the Central Himalaya compared to the sites on the South-Eastern Tibetan Plateau.The yearly cycle of wind speeds (Figure ??d) varies considerably between sites. Common characteristics for~~
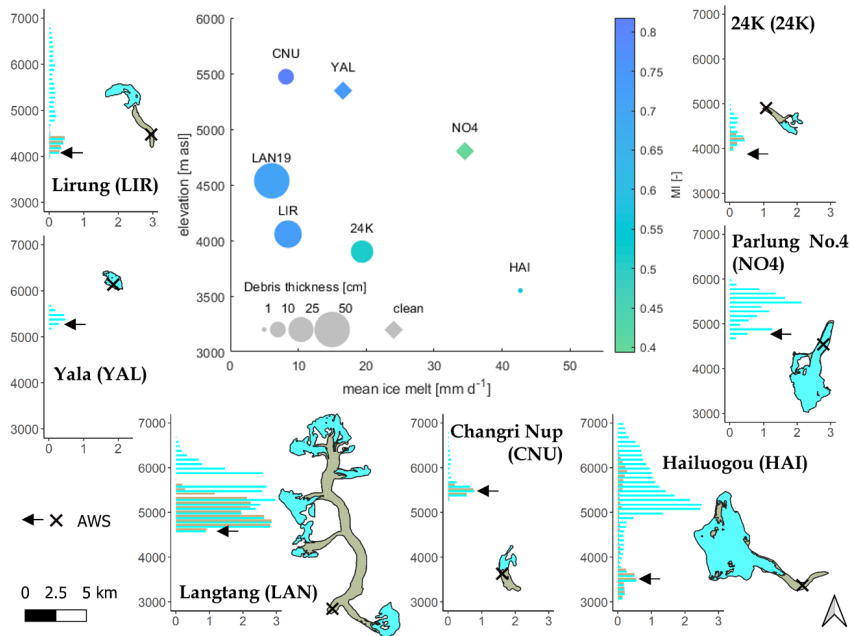
Figure 2. Characteristics of study sites, summarized (center) in terms of elevation, mean measured ice melt rate, measured debris thickness and JJAS contribution to the ERA5-Land total annual (1981-2019) precipitation (monsoon index; MI). For each site, we also show glacier (~~blue~~ in aqua bars) and debris (~~brown~~ in olive bars) hypsometry, with area on the x-axis [km^2] and altitude on the y-axis [$m.asl$], and glacier and supraglacial debris extents. ~~Black crosses and arrows indicate AWS location on the glacier.~~

~~most sites (except for Changri Nup) are that wind speeds are highest around December/January and that monsoonal wind~~
170 ~~speeds are generally higher than during the shoulder seasons. At each site, we define the onset and recession date of monsoon based on visual inspection of the AWS records, observing the seasonal shift of air temperature, relative humidity, and longwave and shortwave radiation. For this, we define the date after which clear shifts are observable in the variables' regime (Figures A3 to A9).~~

~~Monthly climatology derived from ERA5-Land for 1981-2019 (grey background lines), along with the monthly averages~~
175 ~~(black lines) and the study year at each glacier (colored lines). Plotted meteorological variables are **(a)** mean air temperature (Ta), **(b)** incoming shortwave radiation ($SW_\downarrow$), **(c)** incoming longwave radiation ($LW_\downarrow$), **(d)** wind speed (Ws) and **(e)** monthly precipitation sums (Pr). Black vertical lines indicate the average region-wide monsoon season. Boxplots show the monsoon index (MI) over ERA5-Land period as the fraction of monsoonal (June-September) to annual precipitation, with the colored dot indicating the value for the study year.~~

Table 1. Summary of available meteorological and ablation observations at each site, as well as each site's model period. Variables indicated with * were transferred from neighboring weather station. Variables with ** were reconstructed based on other variables measured at the same station.

	\multicolumn{4}{c}{AWS Location}	\multicolumn{3}{c}{Variables measured}	Model period	Reference
	Lat	Lon	Elevation [m.a.s.l.]	Debris thickness [cm]	AWS	Precipitation	Ablation	begin/ end	
Lirung	28.233	85.562	4076	30	$T, RH, W_s, W_d, SW_\downarrow,$ $SW_\uparrow, LW_\uparrow, LW_\downarrow, P_{atm}^*$	Pluvio Kyanging and Yala Basecamp, 3857m.asl and 5090m.asl, hourly, partly lapsed	SR50	2014-05-05/ 2014-10-24	Ragettli et al. (2015)
Langtang	28.279	85.722	4536	50	$T, RH, W_s, W_d, SW_\downarrow,$ $SW_\uparrow, LW_\downarrow^{**}, LW_\uparrow, P_{atm}$	Pluvio Morimoto base camp 4919m.asl, hourly	SR50	2019-05-11/ 2019-10-30	unpublished
Yala	28.233	85.612	5350	-	$T, RH, W_s, W_d, SW_\downarrow,$ $SW_\uparrow, LW_\uparrow, LW_\downarrow, P_{atm}^*$	Pluvio Yala base camp 5090m.asl, hourly	SR50	2019-05-01/ 2019-10-31	ICIMOD (2021)
Changri Nup	27.993	86.780	5470	10	$T, RH, W_s, W_d, SW_\downarrow,$ $SW_\uparrow, LW_\uparrow, LW_\downarrow, P_{atm}^*$	Pluvio at Pyramid meteorological station (4993 m a.s.l.), 4.9 km SE of AWS location, hourly	SR50	2016-05-01/ 2016-10-31/	Wagnon (2021)
24K	27.983	86.778	3900	20	$T, RH, W_s, W_d, SW_\downarrow,$ $SW_\uparrow, LW_\uparrow, LW_\downarrow, P_{atm}^*$	On-glacier tipping bucket, hourly	stake	2016-06-01/ 2016-09-29	Yang et al. (2017)
Parlung No.4	29.761	95.720	4806	-	$T, RH, W_s, W_d, SW_\downarrow,$ $SW_\uparrow, LW_\uparrow, LW_\downarrow, P_{atm}^*$	Pluvio, near terminus 4600m.asl, hourly	stake	2016-05-01 2016-10-31	Yang et al. (2017)
Hailuogou	29.558	101.969	3550	1	$T, RH, W_s, W_d, SW_\downarrow,$ $SW_\uparrow, LW_\uparrow, LW_\downarrow, P_{atm}^*$	Pluvio at GAEORS station, 3000m.asl, 1.5km from terminus	stake	2008-05-15 2008-10-31	Zhang et al. (2011)

Table 2. Characteristics of the study sites. Planimetric glacier and debris surface areas, mean elevation, slope and aspect were calculated using the updated Randolph Glacier Inventory 6.0 by Herreid and Pellicciotti (2020) and the USGS GTOPO30 digital elevation model. Slope (mean) and aspect ~~are mean values~~ (vectorial average) for the whole glacier. MI (~~'~~'Monsoon-Index') is the mean June-September portion of the ERA5-Land total annual precipitation (1981-2019); For Lirung, where the ablation zone has dynamically disconnected from the accumulation zone, the glacier characteristics represent both zones together.

	Area [km^2]		Elevation [$m.asl$]			Slope	Aspect	MI
	Glacier	Debris	min	max	mean	[°]	[°]	[-]
Lirung (LIR)	4.0	1.5	3990	6830	5100	27.6	151.2	0.74
Langtang (LAN)	37.0	17.8	4500	6620	5330	16.0	177.5	0.71
Yala (YAL)	1.4	-	5170	5660	5390	23.5	229.2	0.74
Changri Nup (CNU)	2.7	1.4	5270	6810	5610	15.9	189.4	0.76
24K (24K)	2.0	0.9	3910	5070	4350	18.3	302.6	0.46
Parlung No.4 (NO4)	11.0	-	4620	5950	5330	17.1	23.5	0.40
Hailuogou (HAI)	24.5	4.1	2980	7470	5360	27.0	104.3	0.56

3   Methods

3.1   Tethys-Chloris energy balance model

We use the hydrological, snow and ice modules of the Tethys-Chloris (T&C) land surface model ~~(Fatichi et al., 2012; Mastrotheodoros et al.~~ (Fatichi et al., 2012; Paschalis et al., 2018; Mastrotheodoros et al., 2020; Botter et al., 2020) to simulate the mass and energy balance of the seven study glaciers. The T&C model simulates, in a fully distributed manner, the energy and mass budgets of a large range of possible land surfaces, including vegetated land, bare ground, water, snow and ice. Here, we apply the model at the point scale of the AWS locations to simulate the energy fluxes of the underlying surface and subsurface, which can comprise snow, ice and supraglacial debris cover layers, according to the local and dynamic conditions. The melt and accumulation of ice and snow, and the ice melt under debris are also explicitly simulated. The surface energy balances for the three different possible surfaces are for snow,

$$R_n(T_{sno}) + Q_v(T_{sno}) + Q_{fm}(T_{sno}) - H(T_{sno}) - \lambda E(T_{sno}) - G(T_{sno}) - \underline{dQ}M(T_{sno}) = 0, \tag{1}$$

for debris cover,

$$R_n(T_{deb}) + Q_v(T_{deb}) - H(T_{deb}) - \lambda E(T_{deb}) - G(T_{deb}) = 0, \tag{2}$$

and for ice,

$$R_n(T_{ice}) + Q_v(T_{ice}) - H(T_{ice}) - \lambda E(T_{ice}) - G(T_{ice}) - \underline{dQ}M(T_{ice}) = 0, \tag{3}$$

where $R_n \, [W \, m^{-2}]$ is the net radiation absorbed by the snow/debris/ice surface, ~~$Qv \, [W \, m^{-2}]$~~ $Q_v \, [W \, m^{-2}]$ is the energy advected from precipitation, $Q_{fm} \, [W \, m^{-2}]$ is the energy gained or released by melting or refreezing the frozen or liquid water that is held inside the snow pack, $H \, [W \, m^{-2}]$ is the sensible energy flux and $\lambda E \, [W \, m^{-2}]$ the latent energy flux for any of the surfaces, and $G \, [W \, m^{-2}]$ is the conductive energy flux from the surface to the subsurface. In ice, the conduction of energy is represented in the model down to a depth of $2 \, m$ after which it is assumed the ice pack is isothermal. Finally, ~~$dQ \, [W \, m^{-2}]$~~ $M \, [W \, m^{-2}]$ is the net energy input to the snow or ice pack. For debris on top of ice, and snow on top of debris or ice, the in-/outgoing fluxes towards/from the ice are adjusted according to the respective interface type. The sign convention is such that fluxes are positive when directed towards the surface. To close the energy balance, a prognostic temperature ~~for the~~ T_s is estimated for each computational element. Iterative numerical methods are used to solve the non-linear energy budget equation until convergence for the ice and snow surface, and the heat diffusion equation for the debris surface, while concurrently computing the mass fluxes resulting from snow and ice melt and sublimation. To close the energy balance, a prognostic temperature for the different surface types (T_{sno}, T_{deb}, T_{ice}) is estimated for each computational element. Iterative numerical methods are used to solve the non-linear energy budget equation until convergence for the ice and snow surface, and the heat diffusion equation for the debris surface, while concurrently computing the mass fluxes resulting from snow and ice melt and sublimation. In the case of snow, debris and ice surfaces, either of which is simulated to always fully cover a computational element, T_{sno}, T_{deb} or T_{ice} are equivalent to the element's overall surface temperature T_s. In the following, we

use the surface type specific symbol for surface specific equations, while we use T_s for equations valid for all three surface types.

3.1.1 Radiative fluxes

R_n is calculated as the sum of incoming and outgoing shortwave and longwave fluxes as

$$R_n = SW_\downarrow(1 - \alpha) + LW_\downarrow + LW_\uparrow, \tag{4}$$

where $SW_\downarrow\,[W\,m^{-2}]$ is the incoming shortwave radiation, $\alpha\,[-]$ is the surface albedo, $LW_\downarrow\,[W\,m^{-2}]$ and $LW_\uparrow\,[W\,m^{-2}]$ are the incoming atmospheric and outgoing longwave radiation components, respectively. In this study α is given as an input to the model based on the AWS observations. We prescribe α for all surface types as the daily cumulated albedo, which is the 24 hour sum of $SW_\uparrow$ divided by the sum of $SW_\downarrow$ centred over the time of observation (van den Broeke et al., 2004).

3.1.2 Incoming energy with precipitation

For calculating the incoming energy with precipitation, rain is assumed to fall at air temperature (T_a) when positive, with a lower boundary of 0 °C. Snow is assumed to fall at negative T_a with an upper boundary of 0 °C. Here, Q_v is the energy required to equalize the precipitation temperature with the surface temperature T_s and is therefore calculated as

$$Q_v = c_w\,P_{r,liq}\,\rho_w\,[max(T_a, 0) - T_s] + c_i\,P_{r,sno}\,\rho_w\,[min(T_a, 0) - T_s], \tag{5}$$

where $c_w = 4196\,[J\,kg^{-1}\,K^{-1}]$ is the specific heat of water, $c_i = 2093\,[J\,kg^{-1}\,K^{-1}]$ the specific heat of ice, $\rho_w = 1000\,[kg\,m^{-3}]$ is the density of water and $P_{r,liq}\,[mm]$, $P_{r,sno}\,[mm]$ are the rain- and snowfall intensities, respectively.

3.1.3 Phase changes in the snow pack

The snow pack has a water holding capacity Sp_{wc} described in section 3.2.2. The energy flux gained/released by melting/refreezing the frozen/liquid water that is held inside the snow pack is calculated as:

$$Q_{fm}(t) = \begin{cases} f_{sp}\frac{\lambda_f\,\rho_w\,Sp_{wc}(t-dt)}{1000\,dt}, & T_{sno}(t) < 0 \ and \ T_{sno}(t-dt) \geq 0 \\ -f_{sp}\frac{\lambda_f\,\rho_w\,Sp_{wc}(t-dt)}{1000\,dt}, & T_{sno}(t) \geq 0 \ and \ T_{sno}(t-dt) < 0 \end{cases} \tag{6}$$

where $f_{sp} = \frac{5}{SWE}\,[m^{-1}]$ $f_{sp} = \frac{5}{SWE}\,[]$ with $max(f_{sp}) = 1$ is the fraction of the snowpack water equivalent ($SWE\,[mm\,w.e.]$) involved in either melting or freezing. This choice was made in order to mimic refreezing in the upper portion of the snowpack, while the snowpack is otherwise represented as a single layer. $\lambda_f = 333700\,[J\,kg^{-1}]$ is the latent energy of melting and freezing of water, t stands for time, $dt\,[s]$ is the timestep, and the unit for T_{sno} is $[°C]$.

3.1.4 Turbulent energy fluxes

Over snow, debris and ice surfaces, the sensible energy flux is calculated as

$$H = \rho_a \, C_p \, \frac{(T_s - T_a)}{r_{ah}}, \tag{7}$$

where $T_s \, [°C]$ is the surface temperature (generalised term for $T_{sno}, T_{deb}, T_{ice}$), $C_p = 1005 + [(Ta + 23.15)^2]/3364 \, [J \, kg^{-1} \, K^{-1}]$ is the specific heat of air at constant pressure, $\rho_a \, [kg \, m^{-3}]$ is the density of air. The aerodynamic resistance $r_{ah} \, [s \, m^{-1}]$, which is also a function of wind speed (Ws) is calculated using the simplified solution of the Monin-Obokhov similarity theory (Mascart et al., 1995; Noilhan and Mahfouf, 1996). The roughness lengths of heat ($z_{0h} \, [m]$) and water vapour ($z_{0w} \, [m]$) used in the calculation of the aerodynamic resistance are equal in the T&C model ($z_{0h} = z_{0w}$), and ($z_{0h} = z_{0w} = 0.1 z_{0m}$). The roughness length of momentum (z_{0m}) is set to 0.001 m for snow and ice surfaces (Brock et al., 2000), while we optimize it against the surface temperature for debris (see section 3.3).

Correct estimates of the latent energy flux due to water phase changes at the surface are important to accurately model glacier melt, especially under moist conditions (Sakai et al., 2004). Phase changes between the water and gas phase and the resulting energy fluxes are considered over all surfaces. The latent energy is limited by the availability of water in the form of ice and snow, or in the case of a debris surface, by the amount of water intercepted (interception storage capacity is set to 2mm). The latent energy flux is estimated from:

$$\lambda E = \lambda_s \, \frac{\rho_a \, (q_{sat}(T_s) - q_a)}{r_{aw}}, \tag{8}$$

where λ_s is the latent energy of sublimation defined as $\lambda_s = \lambda + \lambda_f$, with $\lambda = 1000 \, (2501.3 - 2.361 \, T_a) \, [J \, kg^{-1}]$ as the latent energy of vaporisation. q_{sat} is the surface specific humidity at saturation at T_s, q_a is the specific humidity of air at the measurement height and r_{aw} the aerodynamic resistance to the vapour flux, which we assume equals r_{ah}.

Controls on turbulent fluxes
The predictive power of the temperature gradient between surface and air $\delta_T \, [°C^{-1}]$ and Ws as well as their combination for determining H and LE were assessed using a univariate polynomial regression model for the single predictors and a multiple polynomial regression model using both variables, and both models had 2 degrees of freedom.

3.1.5 Ground energy flux

The definition of the ground energy flux $G \, [W \, m^{-2}]$ differs based on the surface type. ~~In the case of~~ When there is snow, it is equal to the energy transferred from the snowpack to the underlying ice or debris surface~~, where in~~. In the assumption of a slowly changing process, G can be approximated with the temperature difference of the previous time step (t-1), which allows to solve for G outside the numerical iteration to find the snow surface temperature of the current time step:

$$G_{sno}(t) = k_{sno} \, \frac{T_{sno}(t-1) - T_{deb,ice}(t-1)}{d_{sno}} \tag{9}$$

where $k_{sno}\,[W\,K^{-1}\,m^{-1}]$ is the thermal conductivity of snow and $d_{sno}\,[m]$ is the snow depth. For ice in the absence of snow and debris, it is the energy flux from the ice pack to the underlying surface or to the ice at a depth of $2\,m$:

$$G_{ice}(t) = k_{ice}\frac{T_{ice}(t-1) - T_{grd}(t-1)}{d_{ice}} \tag{10}$$

where $k_{ice}\,[W\,K^{-1}\,m^{-1}]$ is the thermal conductivity of ice, $T_{grd}\,[°C]$ is the temperature of the underlying ice, and $d_{ice}\,[m]$ is the relevant ice thickness. For debris, which was discretised into eight layers at all debris-covered sites, G is the energy flux conducted into the debris layers. Its calculation is for a given time t and depth z

$$G(z,t) = -k_d\frac{\partial T_{deb}(z,t)}{\partial z_d}, \tag{11}$$

where $k_d[W\,K^{-1}\,m^{-1}]$ is the debris thermal conductivity (see section 3.3) and $T_{deb}(z,t)\,[°C]$ is the debris temperature at time t and depth z. $G(z,t)$ can be included in the heat diffusion equation as such:

$$cv_s\frac{\partial T_{deb}(z,t)}{\partial t} = \frac{\partial}{\partial z_d}(-G(z,t)), \tag{12}$$

where cv_d is the debris heat capacity. Under the assumption of homogeneous debris layers, $\kappa\,[m^2\,s^{-1}]$ as the debris heat diffusivity replaces the term $\frac{k_d}{cv_s}$ and equation (12) can be written as:

$$\frac{\partial T_{deb}(z,t)}{\partial t} = \kappa\frac{\partial^2 T_{deb}(z,t)}{\partial z^2}, \tag{13}$$

The heat diffusion equation (13) is solved using iterative numerical methods. This way, the debris temperature profile $T_{deb}(z,t)$ is solved together with $G(z,t)$ at any depth and time. The conductive energy flux at the base of the debris is used to heat the ice and to calculate ice melt once above the melting point.

Note, that G can also act in the opposite direction, i.e. when energy is conducted from the snowpack/debris/ice towards the surface. In our results, G sums up all types of conductive energy fluxes in the snow-debris-ice column. Part of the energy is used for heating the snow, ice or debris-ice surface layer until melt occurs (G, Table A2).

3.2 Mass balance in the T&C model

3.2.1 Precipitation partition

Input precipitation is required to be Precipitation is partitioned into solid Pr_{sno} and liquid Pr_{liq} precipitation, because of the differing impacts of snow and rain on the energy and mass balance. For this study, the precipitation partition method described by Ding et al. (2014) was implemented into the T&C model. This parameterisation has been developed specifically for High Mountain Asia based on a large dataset of rain, sleet and snow observations, and does not require recalibration. It determines the precipitation partition based on the wet-bulb temperature, station elevation and relative humidity and allows for sleet events, as a mixture between liquid and solid precipitation. Ding et al. (2014) found the wet-bulb (T_{wb}) to be a better predictor than T_a of the precipitation type—. They also found that the temperature threshold between snow and rain increases at higher elevations, and that the probability of sleet is reduced in conditions of low relative humidity.

3.2.2 Water content of the snow, ice and debris layers

The water content of ice is approximated with a linear reservoir model. The liquid water outflow is proportional to the ice pack water content $Ip_{wc} [mm\,w.e.]$, which is initiated when Ip_{wc} exceeds a threshold capacity, prescribed as 1% of the ice water equivalent ($IWE [mm\,w.e.]$). The Ip_{wc} is the sum of ice melt and liquid precipitation, minus the water released from the ice pack. The water released is the sum of the ice pack excess water content plus the outflow from the linear reservoir, given as $I_{out} = Ip_{wc}/K_{ice}$, where K_{ice} is the reservoir constant which is proportional to the ice pack water equivalent. Unlike within snow packs, Q_{fm} is not accounted for within the ice pack, since water is presumed to be evacuated quickly from the ice due to runoff without refreezing.

The water content of the snow pack $Sp_{wc} [mm\,w.e.]$ is approximated using a bucket model, in which outflow of water from the snow pack occurs when the maximum holding capacity of the snow pack is exceeded. Following the method of Bélair et al. (2003), the maximum holding capacity of the snow pack is based on SWE, a holding capacity coefficient and the density of snow rho_{sno}. Snowmelt plus liquid precipitation, minus the water released from the snow pack gives the current Sp_{wc}. If T_{sno} is greater than $0°C$ then the snow pack water content is assumed to be liquid, whereas otherwise it is assumed frozen.

For supraglacial debris, both observations and methods for modelling its water content are lacking. We thus use a simplified scheme for ~~accounting for~~ moisture at the surface of the debris, in order to mimic the drying process of the debris surface: we assume debris to have a dynamic interception storage, which can hold a maximum of $2\,mm$ water at all debris-covered sites and can be refilled by snowmelt or liquid precipitation. The evaporative flux from the debris and the latent energy flux of evaporation is therefore limited by this interception storage.

3.2.3 ~~Glacier~~ Snow and ice mass balance

The mass balance calculation of snow and ice is rather similar, so they will be described together here. Calculations are performed for snow if there is snow precipitation during a timestep or the modelled SWE at the surface is greater than zero. Net input of energy to the snow or ice pack will increase its temperature, and after the temperature has been raised to the melting point, additional energy inputs will result in melt. The change in the average temperature of the ice or snowpack dT is controlled using:

$$dT = \frac{dQ\,dt}{c_i\,\rho_w\,WE_b} \frac{M\,dt}{c_i\,\rho_w\,WE_b} 1000, \tag{14}$$

Where dt is the time step $[h]$ and $WE_b [mm\,w.e.]$ is IWE or SWE before melting and limited to a maximum of $2000\,mm$, assumed to be the water equivalent mass exchanging energy with the surface. Energy inputs into an iso-thermal ice/snow pack result in melt $M [mm\,w.e.]$ as

$$M = \frac{dQM\,dt}{\lambda_f\,\rho_w} 1000 \tag{15}$$

The water equivalent mass of the snow/ice pack after melting $WE(t)\,[mm\,w.e.]$ is updated conserving the mass balance following:

$$WE(t) = WE(t - dt) + Pr_{sno}(t) - E(t)\,dt - M(t), \tag{16}$$

Here $E = \lambda E / \lambda s\,[mm]$ is the sublimation from ice and snow. The snow density is assumed to be constant with depth and calculations are performed assuming one single snow pack layer. The snow density evolves over time using the method proposed by Verseghy (1991) and improved by Bélair et al. (2003). In this parameterisation the snow density increases exponentially over time due to gravitational settling and is updated when fresh snow is added to the snowpack. Two parameters are required in this scheme, ρ_{sno}^{M1} and $\rho_{sno}^{M2}\,[kg\,m^{-3}]$, which represent the maximum snow density under melting and freezing conditions, respectively. The depth of the ice pack can be increased through the formation of ice from the snow pack (ice accumulation), which is prescribed to occur if the snow density increases to greater than $500\,kg\,m^{-3}$ (a density associated with the firn to ice transition) and at a rate of $0.037\,mm\,h^{-1}$ (Cuffey and Paterson, 2010). The density of ice is assumed constant with depth and equal to $916.2\,kg\,m^{-3}$.

3.3 Debris parameters

A major challenge in physically based mass-balance modelling of debris-covered glaciers is the ~~assignment~~ selection of appropriate debris properties. ~~Besides~~ In addition to the debris thickness, which was measured at the AWS location, values are needed for the thermal conductivity k_d, the roughness length z_0 of the debris surface, the surface emissivity ϵ_d, the debris volumetric heat capacity cv_d and and the debris density ρ_d~~have to be assigned~~. While the latter three can be quantified using literature values, there is more uncertainty about k_d and z_0, two highly variable quantities that are difficult to measure in the field~~, but which EB models are highly sensitive to~~. We thus choose to optimize them, since our primary requirement is an accurate representation of the energy and mass balance: (1) in a first step, we optimize k_d simulating only the conduction of energy through the debris during snow free conditions, with the $LW_\uparrow$-derived surface temperature $T_{s,LW}$ as an input, the ice melt as the target variable and the Nash-Sutcliffe Efficieny $NSE\,[-]$ as performance metric. (2) Next, we run the whole energy balance model and optimize z_0 for snow-free conditions, with all required meteorological inputs, and the optimal k_d from step (1), while comparing modelled T_s against $T_{s,LW}$, using NSE as performance metric. The resulting parameters are given in Table 4. All optimized values fall within the expected range based on prior energy-balance studies on debris-covered glaciers (Nicholson and Benn, 2006; Reid and Brock, 2010; Lejeune et al., 2013; Rounce et al., 2015; Collier et al., 2015; Evatt et al., 2015; Yang .

Table 3. Debris parameter values for each site derived from the two-step optimization procedure.

	Lirung	Langtang	Changri Nup	24K	Hailuogou
$k_d\,[W\,m^{-1}\,K^{-1}]$	1.09	1.65	1.77	1.45	0.72
$z_{0m}\,[m]$	0.7	0.38	0.11	0.15	0.027

3.4 Uncertainty estimation

355   We calculate the uncertainty associated with all energy and mass balance components by performing 10^3 Monte Carlo simulations for each study site at the AWS location. We ~~vary~~ perturb three debris parameters (k_d, z_{0m}, ϵ_d), debris thickness h_d, as well as six measured model input variables: air temperature T_a, the ~~vapor~~ vapour pressure at reference height ~~ea[—]~~$ea[Pa]$, $SW_\uparrow$, $SW_\downarrow$, $LW_\downarrow$, the total precipitation before partition Pr, and the wind speed Ws. Measured outgoing shortwave radiation $SW_\uparrow$ was included into the Monte Carlo set, as it determines our input α, as discussed in Section 3.1.1. While the parameter uncer-

360   tainty range was defined based on previously published values for debris ~~(e.g. Yang et al., 2017; Rounce et al., 2015; Evatt et al., 2015; Reie~~ (e.g. Yang et al., 2017; Rounce et al., 2015; Evatt et al., 2015; Reid and Brock, 2010; Nicholson and Benn, 2006; Rowan et al., 2020; Leje , the debris thickness measurement uncertainty was given with a range of ~~1cm~~ $1cm$ and the range for the meteorological inputs was set based on the respective sensor uncertainties (see Table 5). All uncertainties were equally distributed around the standard parameter values and observations. Uncertainties are given as one standard deviation of the error of the Monte Carlo

365   runs against the standard run.

Table 4. Debris parameter values for each site derived from the two-step optimization procedure.

	Lirung	Langtang	Changri Nup	24K	Hailuogou
$k_d \ [W \, m^{-1} \, K^{-1}]$	1.09	1.65	1.77	1.45	0.72
$z_{0m} \ [m]$	0.7	0.38	0.11	0.15	0.027

Table 5. Uncertainty ranges of parameters and input variables used for Monte Carlo runs. Where units are indicated with [-], the parameter or variable was perturbed by the fractional value shown.

Parameter/ Variable	Range	Parameter/ Variable	Range
$k_d\,[-]$	± 0.1	$SW_\downarrow\,[-]$	± 0.03
$z0\,[-]$	± 0.1	$SW_\uparrow\,[-]$	± 0.03
$\epsilon_d\,[-]$	± 0.05	$LW_\downarrow\,[-]$	± 0.03
$h_d\,[mm]$	± 5	$Pr\,[-]$	± 0.15
$Ta\,[°C]$	± 0.2	$W_s\,[m/s]$	± 0.3
$ea\,[-]$	± 0.02		

3.5 Model evaluation

The model accurately reproduces the measured surface height change (ablation and accumulation) at both debris-covered and clean-ice glaciers (Figure 3). The maximum uncertainties associated with each model output ranges from $\pm 4\%$ (Parlung No.4, Figure 3f) to $\pm 15\%$ (Yala, Figure 3c). Where Ultrasonic Depth Gauge (UDG) records are available (Lirung, Langtang, Yala, Changri Nup), the deviations of the simulations from the observations stay within the uncertainty range (Figure 3a-d). We decided to not consider the UDG record from Changri Nup after a large August snowfall, as variables describing the surface state (e.g. α, $LW_\uparrow$) following this event indicate a discontinuous snow cover at the AWS location, while the UDG, which is some meters away from the AWS, shows continuous snow cover with depths of tens of centimeters. This discrepancy was also confirmed by observation of the site from October 2016. It was thus not possible to match the UDG record with the model for the late ablation period on Changri Nup, but the model closely reproduces observed surface height change for the pre-monsoon and early monsoon (Figure 3d), when AWS and UDG observations agree in terms of surface state. The deviation to measured melt is larger than the uncertainty range at 24K and Parlung No.4 for two and one individual stake readings, respectively, but the overall agreement is very good also at these sites (Figure 3e, f). For Parlung No.4 there are no stake measurements available before July 21 due to the long-lasting snow cover.

4 Results

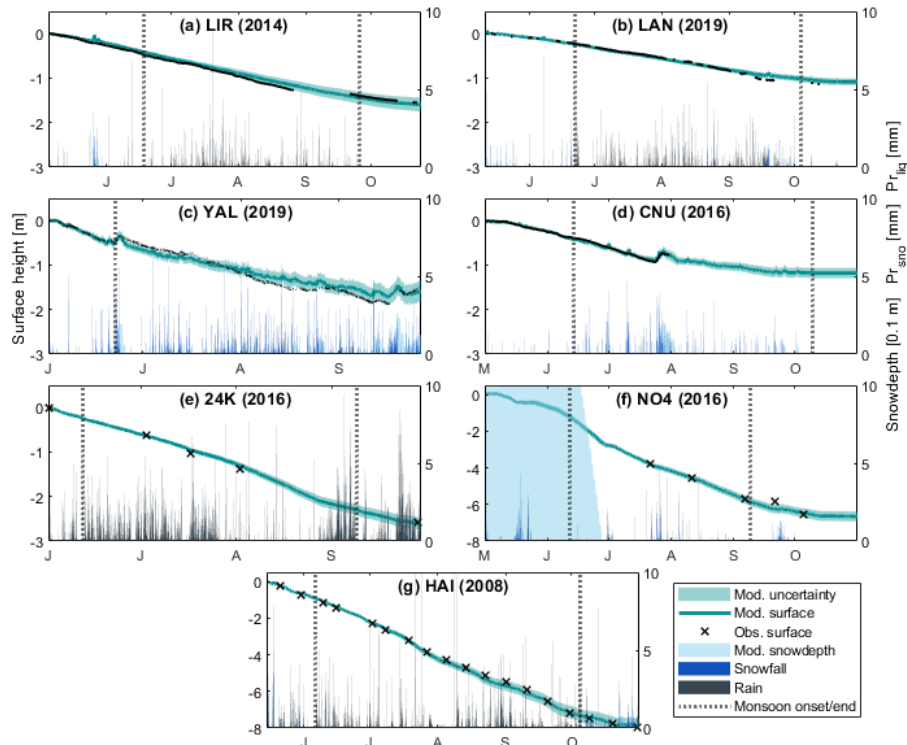### 4.1 Modelled mass balance

Figure 3. (a)-(g) Observed vs. modelled surface change at all study sites, including ice melt, snow melt, sublimation, precipitation phase and snow depth. Measured melt is either from ablation stakes (black crosses) or Ultrasonic Depth Gauges (black lines). Vertical dotted lines indicate monsoon onset and end.

~~The model accurately reproduces the measured surface height change (ablation and accumulation) at both debris-covered~~ The ablation season average melt rates vary considerably across sites: the highest value of $42.7\,mm\,d^{-1}$ is reached at the low-lying site with thin debris cover, Hailuogou, and the lowest value of $6\,mm\,d^{-1}$ is evident at Langtang, a site at moderate elevation but with the thickest debris cover out of all study sites (Figure 4). The largest average seasonal mass loss component at all sites is ice melt, with a minimum of 65.8% of the mass losses at Changri Nup (Figure 4c) and ~~clean-ice glaciers (Figure 3). The maximum uncertainties associated with each model output ranges from ±4% (Parlung No.4, Figure 3f) to ±15% (Yala, Figure 3c). Where Ultrasonic Depth Gauge (UDG) records are available (Lirung, Langtang, Yala, Changri Nup), the deviations of the simulations from the observations stay within the uncertainty range (Figure 3a-d). We decided to not consider the UDG record from Changri Nup after a large August snowfall, as variables describing the surface state (e.g. α~~up to 95.4% at Hailuogou, (Figure 4g). This is followed by snowmelt, ~~$LW_\uparrow$) following this event indicate a discontinuous snow cover at the AWS location, while the UDG, which is some meters away from the AWS, shows continuous snow cover with depths at the order of tens of centimeters. This discrepancy was also confirmed by observation of the site from October 2016. It was thus not possible to match the UDG record with our model for the late ablation period on Changri Nup, but our model closely reproduces observed~~

17

~~surface height change for the pre-monsoon and early monsoon (Figure 3d) , when AWS and UDG observations agree in terms of surface state. The deviation to measured melt is larger than the uncertainty range at 24K and Parlung No.4 for two and one individual stake readings, respectively, but the overall agreement is very good also at these sites (Figure 3e,f). For Parlung No.4 there are no stake measurements available before July 21 due to the long-lasting snow cover.~~~~Mass losses over the ablation seasons (combining ice melt, snow melt and sublimation) show considerable variability between study sites and over time at each site: At all sites, ice melt is the dominant mass loss component,~~ accounting for ~~65.8% (Changri Nup, Figure 4c) to 95.4% (Hailuogou, Figure 4g~~only 0.1% at 24K (Figure 4e) but as much as 33.1% at Yala (Figure 4c) of the ~~total~~ seasonal mass losses. ~~It increases initially during premonsoon at all sites, then tends to plateau at Lirung and Langtang. Snow melt is a smaller component of mass loss, accounting for 0.1% (24K~~Sublimation from ice and snow represents a very small share of the seasonal mass losses, and ranges from 0.01% (Lirung, Figure 4~~e) to 33.1% (Hailuogou~~a) to 1.2% (Changri Nup, Figure 4~~g)of the total mass losses. However, it~~d). It mostly occurs under dry conditions during pre-monsoon at the highest sites (Changri Nup, Yala).

The timing of snow cover is an important control of both amounts and patterns of ice melt, as ice melt rates are ~~suppressed~~ close to zero during periods of snow cover~~(Figure 4). A longlasting~~. This becomes clear in Figure 4, where ice melt rates are low during weeks when also snow melt takes place. A long lasting pre-monsoonal snowpack can delay the onset of ice melt ~~, as~~ considerably, e.g. at Parlung No.4, where ice melt is delayed until the end of June (~~Figure~~ Figures 3f and 4f). Similarly, intermittent snow cover protects the ice from melting at the two highest sites (Yala and Changri Nup) during the summer months (Figure ~~4c and d). Sublimation from ice and snow represents a very small share of the total mass losses, and ranges from 0.01% (Lirung, Figure 4a)to 1.2% (Changri Nup,~~3c-d and 4c-d).

4.2 Modelled energy balance

The largest components in the energy balance are $LW_\uparrow$, $LW_\downarrow$ and $SW_\downarrow$ (Figure ~~4d). It mostly occurs under dry conditions during premonsoon at the highest sites (Changri Nup, Yala). Debris cover is clearly another important control of total mass losses: The presence of debris at least $10\,cm$ thick (Changri Nup, Lirung, Langtang and 24K)causes average melt rates to be comparatively low (8.2, 8.5, 6.1~~ A2). The two longwave fluxes counteract and offset each other in large parts resulting in a moderate, melt-reducing LW_{net}, which reaches its highest values during the pre- and ~~19.4\,mm\,d^{-1}, Figure 4a ,b,d and e), while at the 'dirty-ice' site(Hailuogou, with thin and patchy debris, approximated to be 1 cm), the melt rate is higher (42.7\,mm\,d^{-1}, Figure 4g)over the simulation period, peaking in mid-July. Relatively high average melt rates are also reached at the clean ice sites Parlung No.4 (34.6\,mm\,d^{-1}, Figure 4f) and Yala~~post-monsoon (Figure 5). $SW_\downarrow$ and its reflected counterpart $SW_\uparrow$ result in a net shortwave flux SW_{net}, which at all sites contributes the overall largest amount of energy available for melt M (Figure 5). M is additionally increased or reduced by the turbulent fluxes H and LE, while the energy advected to the glacier surface by precipitation (Qv) remains small $(< 2\,W\,m^{-2}$, Table A2). G links the snow/debris/ice surface to the subsurface, and is a result of all surface fluxes and the subsurface conditions. Before ice melt occurs, depending on season and site, a part dG of G between 0 and $17.8\,W\,m^{-2}$, is invested into warming the debris or ice pack to the melting point (Table A2). dG tends to
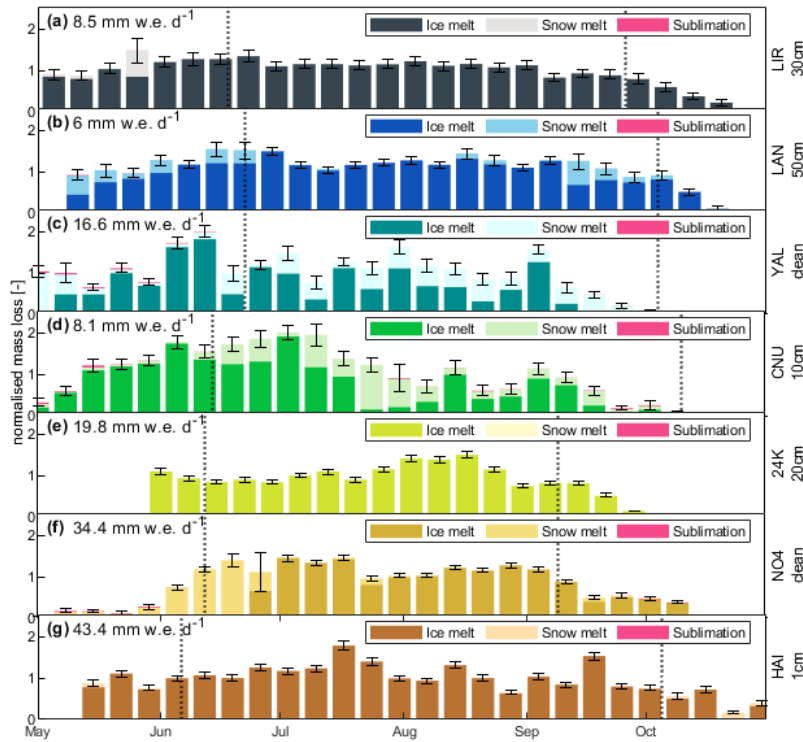
Figure 4. (a)-(g) Melt rates of ice and snow (stacked) as weekly averages at each site. Vertical dotted lines indicate monsoon onset and end. Error bars depict the uncertainty (standard deviation) of the estimates. Melt rates are normalized to the mean of the ice melt over the entire period (value in the upper left of each panel).

be larger during pre-monsoon and at the higher sites (~~16.6 $mm\,d^{-1}$, Figure 4c), despite the high altitude of the latter.~~ Yala,
430 Changri Nup), where ambient temperatures frequently fall below $0\,^{\circ}C$.

~~(a)-(g) Melt rates of ice and snow (stacked) as weekly averages at each site. Vertical dotted lines indicate monsoon onset and end. Error bars depict the uncertainty (standard deviation) of the estimates. Melt rates are normalized to the mean of the ice melt over the entire period (value in the upper left of each panel).~~

4.3 ~~Modelled energy balance~~Impact of debris cover

435 ~~The main energy source on all glaciers and during all seasons is SW_{net} (Figure 5) . At all sites and over the entire modelling period, LW_{out} is the largest energy sink, but it remains comparably stable in magnitude between the seasons (Figure **??**). The turbulent heat fluxes (~~ Debris cover modulates the energy balance in several ways: with the albedo of the snow free debris surface ranging between 0.05 (24K) and 0.22 (Changri Nup), a much larger amount of $SW_{\downarrow}$ is absorbed by the surface than on clean ice glaciers, where the albedo typically ranges between 0.3 and 0.6. In contrast to clean-ice glaciers however, where the
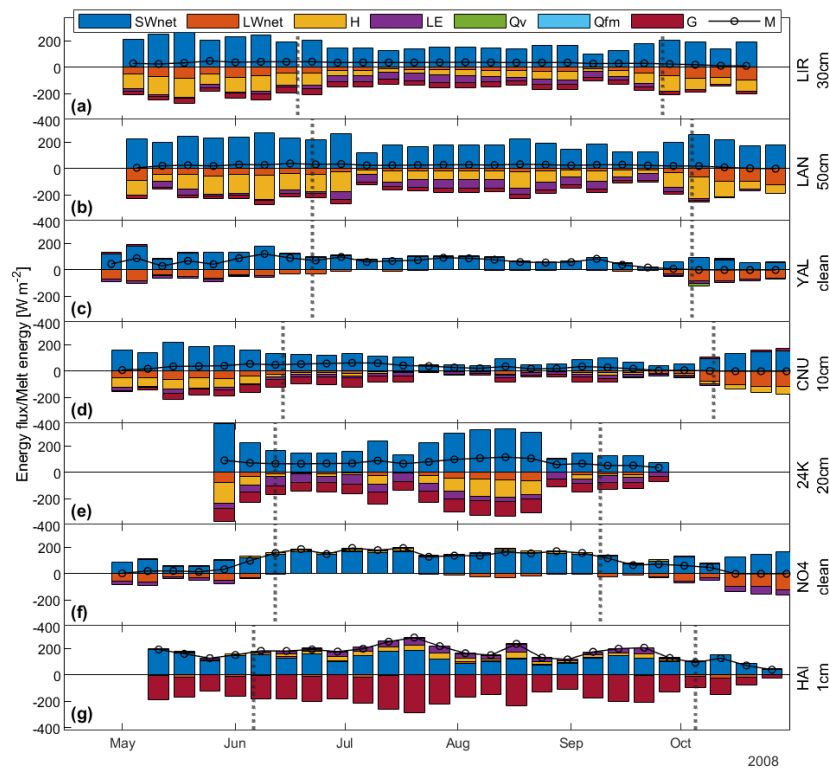
19

Figure 5. (a)-(g) ~~Measured vs. modelled surface change~~ Stacked energy fluxes weekly averages at ~~all study sites~~each site, ~~including ice melt~~depicting the components SW_{net}, ~~snow melt~~LW_{net}, ~~sublimation~~H, ~~precipitation phase~~LE, Q_v, Q_{fm}, G and ~~snow depth~~M. ~~Measured melt is either~~ Energy fluxes are negative fluxes when directed away from ~~ablation stakes (black circles) or Ultrasonic Depth Gauges (black lines). Vertical dotted lines indicate monsoon onset~~ the surface and ~~end~~positive when directed towards the surface.

440   main flux re-emitting absorbed energy is $LW_\uparrow$ (Figure 5c and f), a large part of the debris-absorbed energy is also re-emitted to the atmosphere by the turbulent fluxes H and LE ~~), and dQ (G on debris) act as energy sinks on average at all sites. G can however act in both ways,as an energy source when warming the glacier,and as an energy sink when warming the air. In our definition G sums up all types of conductive energy fluxes in the snow-debris-ice column. Part of the energy is used for heating the snow, ice or debris-ice surface layer until melt occurs (dG, Table A2) . The relative contributions of the individual sinks~~

445   ~~strongly depends on the surface type: LW_{net} is an important sink at the~~ (Figure 5a,b,d and e). As a result of this insulating effect of debris, the seasonal average melt rate of debris-covered 24K is considerably lower ($19.8\ mm\,d^{-1}$) than that of clean-ice ~~sites, while the turbulent fluxes remain small there. On~~ Parlung No.4 ($34.4\ mm\,d^{-1}$), despite the latter site being 900 m lower in elevation than the former one (Figure 4e and f), and their geographical proximity (1). On Hailuogou, the site with very thin debris however, the ~~debris-covered glaciers with debris >10 cm thick, where LW_{net} plays a relatively small role, the~~

450   turbulent fluxes act ~~as major energy sink. Where debris is thin, they instead act as additional energy sources.In the following, we consider how energy fluxes change when moving from pre-monsoon to monsoon. Note that the sign of this change depends~~

~~on the sign of the original flux, which is negative when the flux acts as an energy sink (energy away from the surface)and positive when the flux acts as a source (energy towards the surface). As an example, a negative change in LE, when acting as a sink, means an increase in its magnitude.The seasonal imprint of the monsoon on the energy balance is very clear at all study sites on average and diurnally: There is a strong reduction in the magnitude of~~ in the opposite direction, i.e. contributing energy for melt. Summed up, they can reach weekly averages of $150\,W\,m^{-2}$ (Figure 5g).

4.4 Impact of the monsoon

During monsoonal conditions, increased cloudiness results in $SW_\downarrow$ ~~during monsoon across sites (with decreases~~ decreasing its melt contribution at all sites compared to pre-monsoonal conditions (Figure 6) with changes ranging between -41.8 ~~and $-135\,W\,m^{-2}$~~ (Hailuogou, pre-monsoon: 178.2; monsoon: 136.4) and -135 (Yala, pre-monsoon: 307.7; monsoon: 172.7) at the seven sites ~~, Figure 6 and~~ (all values in $W\,m^{-2}$, from Table A2)~~, which however remains the main energy source.~~. Note that we express fluxes in terms of the net energy absorbed by, or removed from the snow/debris/ice surface, (with positive and negative fluxes indicating energy absorbed and removed from surface, respectively). Reflected shortwave radiation $SW_\uparrow$, which ~~is a sink controlled by~~ removes energy from the surface, and which is controlled by the surface albedo, follows these changes (~~ranging from~~ Figure 6), becoming less negative by $+5.4$ ~~to $+164.8\,W\,m^{-2}$ between sites) with the exception of~~ (24K, pre: -18.5, mon: -13.8) and up to $+164.8$ (Parlung No.4, pre: -219.6, mon: -54.8) between sites. An exception to this is Changri Nup, where $SW_\uparrow$ ~~increases in magnitude (~~changes by $-12.1\,W\,m^{-2}$ ~~, Table A2)~~(pre: -60.6, mon: -72.7), an increase of the flux as a consequence of ~~ephemeral~~ the high albedo of ephemeral monsoonal snow cover (Figure 3~~). $LW_\downarrow$ on~~ e, Table A2). On the other hand, the melt contribution of $LW_\downarrow$ increases at all sites (~~by~~ Figure 6), by at least $+15.7$ ~~to $+57.0\,W\,m^{-2}$), and~~ (Hailuogou, pre: 314.6, mon: 330.3) and up to $+57.0$ (Yala, pre: 248.5, mon: 305.5) (Table A2). Its counterpart $LW_\uparrow$ ~~slightly increases in magnitude as well (~~further reduces melt, but to a lesser extent, by -1.0 (Changri Nup, pre: -318.7, mon: -319.7) to ~~$-13.3\,W\,m^{-2}$) (Figure 6 and~~ (Langtang, pre: -339.3, mon: -352.8) (Table A2). ~~At the debris-covered sites , the reduction in R_{net}~~ As a result LW_{net} plays only a minor role in cooling the glaciers at all sites during monsoon (Figure 5).

4.4.1 Impact of the monsoon on clean-ice sites

We observe opposite changes in M at the two clean-ice glaciers in the transition from pre-monsoon to monsoon~~is balanced by a reduction in the magnitude of H (with changes of $+15.6$ to $+67.7\,W\,m^{-2}$ between sites) , which acts as a major energy sink during both sub-seasons (Figure 5, 6 and~~: M decreases at Yala by -10.2 (pre: 74.8, mon: 64.6) and increases at Parlung No.4 by $+130.4$ (pre:32.3, mon: 162.6) (all values in $W\,m^{-2}$, from Table A2). ~~LE, which plays a small role as a sink compared to H during pre-monsoon, increases in magnitude at the debris-covered sites (with changes ranging from -2.7 to $-24.4\,W\,m^{-2}$, Figure 6 and~~ LW_{net} evolves in similar ways at the two sites and as described in Section 4.4. The difference in M is largely caused by the variability in SW_{net}, which almost entirely controls the melt of the clean-ice glaciers during monsoon. Both H and LE on average remain small energy fluxes at the clean ice sites with highest averages of $LE = -17.6$ at Parlung No.4 and of $H = -13.7$ at Yala (Table A2)~~, and acts as a considerable heat sink during the monsoon. As a result of~~
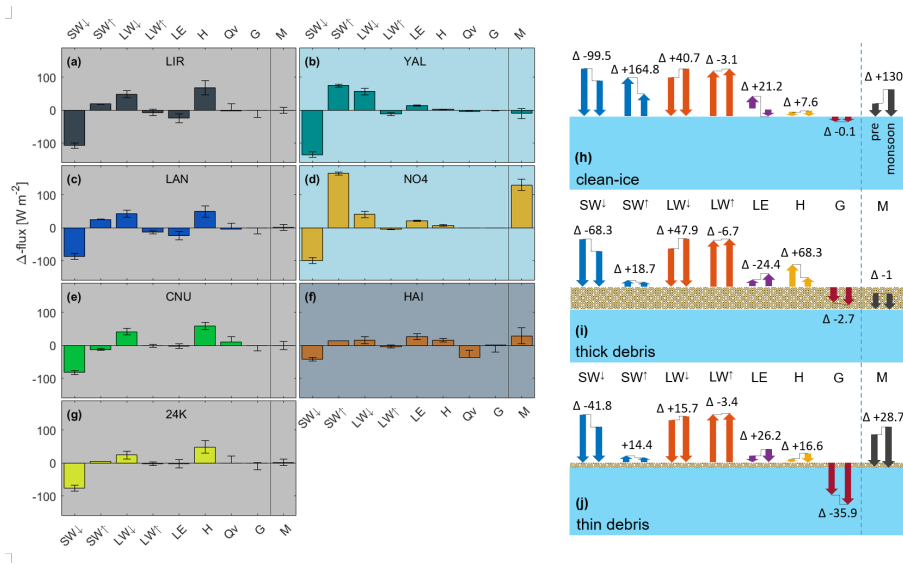
Figure 6. (a)-(g) Differences in energy balance components from pre-monsoon to monsoon at each site including their uncertainties (error bars). The direction of change is to be considered relative to the sign of the original flux (x-axis). Due to the sign convention mentioned in Section 4.3, the presented changes reflect whether the surface receives more energy (positive change) or less energy (negative change). Background indicates the surface type of the site: gray indicates thick debris cover, light blue indicates clean-ice sites, and grey-blue indicates thin debris. **(h)-(j)** Alternative depiction of the changes from (a)-(f), summarizing surface types; Example Δ-flux numbers in [W m-2] refer to (h) Parlung No.4, (i) Lirung and (j) Hailuogou; Numbers for the remaining glaciers can be looked up in Table A2.

these contrasting changes, dQ remains fairly . Interestingly, LE changes from being an evaporative, melt-reducing energy flux
485   during the pre-monsoon, to a small melt-contributing energy flux ($< 4\,W\,m^{-2}$) at both clean-ice sites (Table A2).

4.4.2   Impact of the monsoon on glaciers with thick debris

Average M remains similar between the pre-monsoon and monsoon at the debris covered sites (with changes ranging between +1.3 and −3.3 $W\,m^{-2}$) sites with thick debris cover, as the energy balance components adjust to monsoonal conditions: the changes in M, ranging between −1.0 (Lirung, pre: 37.5, mon: 36.5) and +2.1 (24K, pre: 79.5, mon: 81.6), stay below
490   uncertainty levels (all values in $W\,m^{-2}$, Figure 6a, c, e, g and Table A2). This is partly a consequence of a compensation between increased/reduced melt rates before/after noon (Figure A11). An exception is the thin-debris site Hailuogou, where dQ increases in magnitude (by −26.2 $W\,m^{-2}$), mostly as a result of warmer nights (Figure A11). At the clean-ice sites, $LW_\downarrow$ is initially larger than $LW_\downarrow$ in the pre-monsoon, but the two become almost equal while adjusting to monsoon conditions, causing the LW_{net} to be close to zero ($LW_\downarrow$: +40.7 to +57.0 $W\,m^{-2}$, and $LW_\uparrow$: −3.1 to −11.7 $W\,m^{-2}$) , Table A2 and Figure 5e
495   and f). LE switches sign when moving from pre-monsoon to monsoon, becoming a small condensation energy flux (Yala: 0.1, Parlung No.4: 3.8 $W\,m^{-2}$) . So does Similar to the other surface types, LW_{net} reduces melt to a lesser degree during the monsoon (Section 4.4). There is a considerable reduction in the melt-contribution of SW_{net}, and the glacier-cooling H at

22

Yala, becoming a small heat source instead of a heat sink (0.5 $W\,m^{-2}$, Table A2), while at Parlung No.4, H is a heat source across the seasons (pre-monsoon: 4.9 $W\,m^{-2}$, monsoon: 12.7 $W\,m^{-2}$, becomes a smaller flux by 49.0 (24K, pre: -99.8, mon:

500 -50.8) up to 68.3 (Lirung, pre: -116.7, mon: -48.4) (Table A2). The change in LE partly offsets the changes in H, with increases in the flux ranging from -2.1 (24K, pre: -50.6, mon: -52.7) to 24.4 (Lirung, pre: -16.0, mon: -40.4) (Figure 6a, c, e and g, and Table A2). The turbulent fluxes, however, remain comparably small in magnitude at the clean ice sites (Figure 5c and f). dQ increases in magnitude at Parlung No.4 from pre-monsoon to monsoon (by $-131.0\,W\,m^{-2}$) and decreases in magnitude at Yala (by $-10.2\,W\,m^{-2}$) (Figure 6b and d). Both changes are consequences of snow cover, prevalent during

505 Therefore, the changes in the fluxes from the pre-monsoon at Parlung No.4 and during monsoon at Yala (Figure 3e and fto monsoon tend to balance each other out (although $SW_{\downarrow}$ decreases, $LW_{\downarrow}$ increases, and although H reduces, LE increases), so that overall melt rates remain similar.

An interruption of the monsoon at 24K occurred in August 2016, possibly associated with an El Niño event (Kumar et al., 2006) . During this interruption the energy balance returned to a pre-monsoonal regime (Figure 5e) due to clearer skies, more

510 pronounced diurnal temperature amplitudes, low precipitation rates and lower relative humidity (Figure A7), resulting in higher melt rates during that period (Figure 4e).

Hailuogou, our 'dirty ice glacier', behaves entirely differently compared to both debris-covered and clean sites, with the

4.4.3   Impact of the monsoon a glacier with thin debris

In contrast to the glaciers with thick debris, during the monsoon, the melt energy M increases considerably at Hailuogou

515 Glacier. Although SW_{net} contributes less energy for melt during the monsoon and LW_{net} remains overall small at this site (Figure 5), M increased by 28.7 (pre: 158.1, mon: 186.8) on average (all values in $W\,m^{-2}$, from Table A2), and mostly during the nights (Figure A11). The increase in melt energy is mostly driven by the turbulent energy fluxes increasing in magnitude to become considerable heat sources during monsoon (H: $+15.6\,W\,m^{-2}$ fluxes: H increases by 16.6 (pre: 9.1, mon: 25.7) and LE increases by 26.6 (pre: 5.4 mon: 31.6) (Figure 5 and LE: , $+24.5\,W\,m^{-2}$), driving a pronounced increase in the energy

520 available for melt (dQ: $-26.2\,W\,m^{-2}$, Figure 5, 6 and Table A2)., with higher increases during the nighttime than during the daytime (Figure A11). While they act to reduce melt at the glaciers with thick debris cover, here the turbulent fluxes drive additional melt during the monsoon.

4.5   Turbulent fluxes at debris-covered sites and their controls

The turbulent fluxes LE and H are important heat sinks on

525 ### 4.5   Controls on the turbulent fluxes

Our results show the importance of the turbulent fluxes in the energy balance of debris-covered glaciers and heat sources on the dirty-ice glacier, while they remain small on the clean-ice glaciers (Figure 5). Their magnitude largely determines the energy that is conducted into the debris and used for ice melt . We observe a decrease in the magnitude of H and an increase in the

magnitude of LE ~~going from pre-monsoon to monsoon at the debris-covered~~ glaciers, ~~while both increase as sources of energy~~

530 ~~at the dirty-ice glacier (Figure 6). The predictive power of the temperature gradient between surface and air $g_T [°C^{-1}]$ and~~ ~~Ws as well as their combination for determining H and LE were assessed using a univariate polynomial regression model~~ ~~for the single predictors and a multiple polynomial regression model using both variables, and both models had 2 degrees of~~ ~~freedom~~their varying role as melt-enhancing or melt-reducing fluxes depending on the debris thickness, and how the monsoon modulates them.

535 From the regression models (Section 3.1.4), we find that H ~~is largely controlled by the temperature gradient between surface~~ ~~and air (g_T)on debris-covered glaciers, which explains between 75 and 99% of the variability of H (Figure 7), and g_T decreases~~ ~~during monsoonal conditions by -0.05 to $-1.44\,°Cm^{-1}$ (Table A3). Here it is clear that a smaller temperature gradient~~ ~~between surface and air during the monsoon reduces the magnitude of H as a sink. H~~ is largely controlled by the temperature gradient between surface and air (g_T ~~) on debris-covered glaciers , which explains between 75 and 99%~~ δ_T) on glaciers with

540 thick debris: between 73 (Lirung, pre-monsoon) and 98% (24K, pre-monsoon) of the variability of H are explained by δ_T (Figure 7a), and ~~g_T~~ δ_T decreases during monsoonal conditions by -0.05 (Langtang) to $-1.44\,°Cm^{-1}$ (Changri Nup) (Table A3). ~~Here it is~~ It becomes clear that a smaller temperature gradient between surface and air during the monsoon ~~reduces the~~ ~~magnitude~~ weakens the melt-reducing effect of H ~~as a sink. Wind~~ . In contrast, Ws emerges as the most important control of H ~~at the dirty-ice glacier~~ and LE at the glacier with thin debris, explaining up to 89 ~~% of variability~~ and 65% of the variability,

545 respectively (Figure 7a). The mean magnitude of Ws increases at ~~that site from $1.23\,ms^{-1}$~~ this site from 1.23 in pre-monsoon to ~~$2.10\,ms^{-1}$~~ $2.1\,ms^{-1}$ in monsoon (Table A3). A cold surface in combination with a wind-enhanced turbulence and fast turnover of warm ~~air mass results in~~ and moist air masses results in both H ~~becoming a potent heat source on the dirty-ice~~ ~~glacier. From a physical perspective, the same holds for clean-ice glaciers experiencing simultaneously high wind speeds and~~ ~~high air temperatures. This is, however, not observed on Yala and Parlung No.4, where air temperatures stay comparably low~~

550 ~~and average wind speed decreases slightly in monsoon compared to pre-monsoon (Table A3~~and LE becoming powerful drivers of melt on Hailuogou, the glacier with thin debris cover (Figure 5).

Neither RH, g_T, or Ws on their own, nor their combination explain the variability of LE across sites with thick debris (Figure 7a). LE however increases consistently from pre-monsoon to monsoon together with an increase in the duration of moisture availability at the surface of ~~debris-covered glaciers(by 21 to 63%,~~ those glaciers, with increases ranging between 22.3% at 24k

555 and 63.1% at Changri Nup (Table A3). In fact, evaporation and ~~the related~~ its melt-reducing LE ~~release tends~~ flux tend to be water-limited during the pre-monsoon, but energy-limited during the monsoon (Figure ~~??~~7b). This implies that the availability of ~~moisture is driving~~ additional moisture drives the increase of LE from pre-monsoon to monsoon.~~However, on the dirty-ice~~ ~~glacier, LE acts as a heat source across sub-seasons and switches sign during monsoon at the clean-ice sites. This happens when~~ ~~T_a is consistently higher than T_s, causing condensation when the warm air touches the cold glacier-, or thin debris-surface.~~

560 ~~(a)-(g) Stacked energy fluxes weekly averages at each site, depicting the components SW_{net}, LW_{net}, H, LE, Q_v, Q_{fm}, G~~ ~~and dQ. Energy fluxes are negative fluxes when directed away from the surface and positive when directed towards the surface.~~
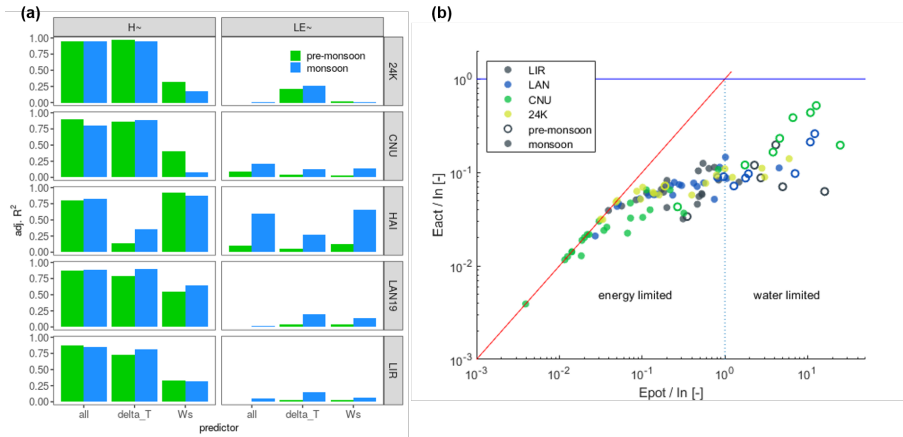
Figure 7. ~~(a)-(g)~~ ~~Differences in energy balance components from pre-monsoon to monsoon at each site including~~ **(a)** Predictive power of temperature gradient between surface and air (δ_T) and wind speed (Ws) and their ~~uncertainties~~ combination (~~error bars~~'all') for determining H and LE. ~~The direction~~ A multiple polynomial regression model including both variables was used, otherwise a univariate polynomial regression model, and both models had 2 degrees of ~~change is to be considered~~ freedom. **(b)** Budyko-like diagram with the 5-day mean potential evaporation rate during snow-free conditions ($Epot$) relative to the ~~sign of the original flux~~ mean available intercepted water (~~x-axis~~ In) ~~. For example, a positive change in a negative flux means a reduction in~~ on the ~~flux~~ x-axis, and ~~can also lead~~ the actual evaporation rate during snow-free conditions ($Eact$) relative to ~~a change in sign. Background indicates~~ In on the ~~surface type of the site: grey indicates~~ y-axis. Only debris-covered ~~glaciers, light blue indicates clean-ice sites~~ where LE is a glacier-cooling flux, ~~and grey-blue indicates thin-debris~~ are shown.

~~Budyko diagram with the 5-day mean potential evaporation rate during snow-free conditions ($Epot$) relative to the mean available intercepted water (In) on the x-axis, and the actual evaporation rate during snow-free conditions ($Eact$) relative to In on the y-axis. Only debris-covered glaciers, where LE is a sink term on average, are shown.~~

565

5 Discussion

5.1 ~~Monsoon effects~~Which mass and energy fluxes determine the seasonal mass balance of glaciers in the Central and Eastern Himalaya?

570 ~~Monsoon impacts on glaciers are complex and spatially variable along the Himalayan arc. The varying strength of~~ We apply our model in a systematic way to seven glaciers in a variety of environments in the Central and Eastern Himalaya. We force the model with in-situ station data and constrain and evaluate it against observations of surface height change, lending great confidence to the energy flux components. Previous energy balance studies in the region were limited to two (Lejeune et al., 2013; Yang et al., 2017; Bonekamp et al., 2019) or three (Zhu et al., 2018) study sites, and partly relied on reanalysis

575 products or atmospheric modelling for forcing (Zhu et al., 2018; Bonekamp et al., 2019), without the possibility to evaluate the model performance. At all our study sites, ice melt is the largest mass loss component during the ablation season, followed by snow melt, while sublimation plays only a small role early and late in the ~~monsoons reflect in the distinct meteorological seasonality between our study sites~~(Figure ??). ~~The ablation period occurs between April and November at all sites, and all sites are affected by the Indian and East Asian summer monsoons during this period (Figures A3 to A9). On average, 70 to~~

580 ~~85% of precipitation arrives during the summer months (June-September) at our Central Himalayan sites (Lirung, Lantang, Yala and Changri Nup, Figure ??a-d) in contrast to 40 to 55% at the eastern sites (24K, Parlung No.4 and Hailuogou, Figure ??e-g).~~

5.1.1 ~~All glaciers~~

~~Overcast conditions caused by monsoon increase $LW_\downarrow$ and with that the magnitude of T_a at all sites (Figures A3 and 6). $SW_\downarrow$~~

585 ~~on the other hand is reduced at all glacier surfaces due to the reflection and scattering of persistent, heavy clouds. While the changes of these two primary sources of energy partly counteract each other in terms of energy supply to glacier surfaces during monsoon,~~ season (Section 4.1). Similar to several previous studies (~~??~~Yang et al., 2011; Sun et al., 2014), we find that ~~net incoming radiation decreases in magnitude everywhere. Another major control~~ the largest energy source for snow and ice melt is SW_{net} (Section 4.2). Thus, major controls on the energy and mass balance of all glaciers are the snowcover dynamics

590 (Zhu et al., 2018) and the associated variations in albedo, which in turn are ~~driven by the precipitation seasonality~~ modulated by the timing of precipitation and the partition of precipitation into rain and snow (Ding et al., 2017; Bonekamp et al., 2019). For example, in the case of Parlung No.4, the onset of glacier melt was delayed until well after monsoon onset, until all snow had disappeared (~~Figure 4~~Section 4.1). After snow has melted out, ephemeral snowcover from monsoonal precipitation ~~increases~~ increased surface albedo and ~~raises~~ raised $SW_\uparrow$, protecting the ice and suppressing melt rates throughout the summer

595 ~~. This is especially relevant at high elevation~~ (Fujita and Ageta, 2000) (Section 4.1). This was especially true at the highest sites (Yala, Changri Nup)~~. An interruption of~~, highlighting the importance of observations of high-elevation surface condition for constraining seasonal glacier mass balance.

5.2 How does debris cover modulate the energy balance in comparison to clean-ice surfaces?

Previous energy balance studies on debris-covered glaciers were limited to one or two study sites (e.g. Lejeune et al., 2013; Collier et al., 20 . Applying the model at five sites with debris cover allows us to identify processes that are likely to be common for a large population of debris-covered glaciers in High Mountain Asia. At the four sites with thick debris, our work confirms that debris protects the ice by returning energy to the atmosphere in the form of turbulent fluxes H and LE in addition to $LW_\uparrow$ (Yang et al., 2017) and that the turbulent fluxes can be a major component in the energy balance during both dry and wet conditions (Steiner et al., 2018) (Section 4.3). We also find a melt-enhancing effect of thin debris (Östrem, 1959; Reznichenko et al., 2010; at Hailuogou Glacier (Section 4.4.3), and that the turbulent fluxes "work against" this glacier (Section 4.5). Our analysis extends beyond most prior representations however by including a water interception storage (Section 3.2.2), which is capable of mimicking the drying process of the debris (Steiner et al., 2018). Representing this process, which was often neglected in previous studies, allows for a more realistic estimation of LE, which is crucial in it's role as a glacier-cooling flux at the glaciers with thick debris, and as a control of potential melt enhancement of thin debris (Evatt et al., 2015). Uncertainty remains around the size of the interception storage - for this study it was fixed to 2mm - and investigations on the water interception and holding capacity of debris are needed in order to elucidate this process. It's representation however allows us to extend the short-period results of (Steiner et al., 2018) to multiple sites and across distinct meteorological conditions, emphasizing the importance of turbulent fluxes for debris-covered glacier energy balance. In contrast to the ~~monsoon at~~ debris-covered glaciers, the turbulent fluxes play a minor role on the clean-ice glaciers (Section 4.4.1).

5.3 How does the monsoon change the glacier surface energy balance?

The ablation period occurs between April and November at all sites, and all sites are affected by the Indian and East Asian summer monsoons during this period (Figures A3 to A9). A long-term average of 65 to 85% of precipitation arrives during the summer months (June-September) at the Central Himalayan sites (Lirung, Lantang, Yala and Changri Nup, Figure A1a-d and Table 2) in contrast to 40 to 56% at the eastern sites (24K~~occurred in August 2016, possibly associated with an El Niño event (Kumar et al., 2006). During this interruption the energy balance returned to a pre-monsoonal regime of clearer skies, more pronounced diurnal temperature amplitudes, low precipitation rates and lower relative humidity (Figure A7), resulting in higher melt rates during that period (Figure 5e).~~, Parlung No.4 and Hailuogou, Figure A1e-g and Table 2). $SW_\downarrow$ is reduced at all glacier surfaces due to the reflection and scattering by persistent, heavy clouds (Figure 8). Overcast conditions caused by monsoon also increase $LW_\downarrow$ at all sites (Figure 8). Our analysis shows that some effects of monsoon are common for all surface types, while the presence or absence of debris and its thickness control how the incoming energy is absorbed and transmitted to the ice ~~.~~ (Figure 8). We therefore provide a synthesis of the changes based on surface types:

5.3.1 ~~Debris-covered glaciers~~

~~Monsoon conditions in combination with debris cover affects the energy balance in a way that stabilizes melt rates over the ablation period, despite~~

5.3.1 Glaciers with thick debris

Overcast cloud cover, increasing air temperatures ~~typical of monsoon (Figure 5). Enhanced melt during the night and morning in monsoon, resulting from higher T_a, is partly offset during the cooler afternoon hours (Figure A11) when the wet air masses usually arrive in this region, bringing intense cloud-cover and precipitation. While~~ and additional moisture modify the energy balance of debris-covered glaciers, to result in a melt-equalizing effect (Section 4.3): warm clouds emit additional amounts of energy towards the glacier in the form of $LW_\downarrow$ (Figure 8, Section 4.4). H ~~decreases~~ reduces its cooling effect as a consequence of a smaller average temperature gradient between surface and air ~~, more latent energy is released from the~~ (Figure 8, Section 4.5). On the other hand, additional evaporative cooling in the form of LE takes place at the wet debris surface, ~~which~~ balancing out the other, melt-enhancing changes (Figure 8, Section 4.3). The debris surface shifts from a water-limited ~~process~~ environment during pre-monsoon to an energy-limited process during monsoon (~~Figure ??). It has been known from studies at individual sites that debris cover protects the ice by returning energy to the atmosphere in the form of turbulent fluxes (Yang et al., 2017) and that the turbulent fluxes can be a major component in the energy balance during both dry and wet conditions (Steiner et al., 2018). Accounting~~ Section 4.5 and Figure 7). We account for the debris water content through the inclusion of a simple interception storage ~~has~~ (Section 3.2.2). This allowed us to identify the importance of the ~~latent heat flux in the cooling effect of evaporation from debris during monsoon, a process that has often been neglected in previous modelling studies. We have been able to quantify how cloud overcast and additional moisture modify the energy balance of debris-covered glaciers, and especially the turbulent fluxes, to result in a melt-equalizing effect~~ glacier-cooling LE coming from the evaporation of liquid water from the debris. Our results are derived from simulations at one location (AWS) on each glacier. To understand how representative our results are of conditions across the glacier ablation zone at each site, and across the possible range of debris thicknesses in particular, we conduct a sensitivity experiment to evaluate the transferability of our results across the glaciers' ablation areas (see detailed explanation in Section A1). This experiment shows that even accounting for the range of conditions across each glacier ablation area, the pattern of pre-monsoon to monsoon difference in flux components, and importantly the equalizing effect on M, remain similar at the glacier scale at all sites with thick debris cover.

5.3.2 Clean-ice glaciers

In contrast to debris-covered glaciers, when clean-ice glaciers are snow-free and the ice has been heated to the melting point, almost all net radiation ~~leads directly to~~ goes into ice melt, while the turbulent flux contribution remains small ~~. When~~ (Section 4.4.1). However, when entering the monsoon period, ~~the latent heat flux switches sign~~ LE tends to switch sign (Figure 8), changing from sublimation/evaporation to condensation, which adds energy to the surface instead of removing it (Section 4.4.1). This behaviour has ~~previously been observed at sites with a 'southern influence' (Yang et al., 2017; Azam et al., 2014)~~ ~~, but has~~ not been indicated for the drier conditions on the Tibetan Plateau (Mölg et al., 2012; Sun et al., 2014)~~.~~, but has previously been observed at Himalayan sites with a 'southern influence' (Azam et al., 2014; Yang et al., 2017). In contrast to

the glaciers with thick debris, the energy balance of clean-ice glaciers is highly sensitive to elevation, as shown in our sensitivity experiment (Section A1)

5.3.3 ~~Dirty-ice glacier~~Glacier with thin debris

665 At ~~our~~ the site with thin debris, ~~the effects that we have observed for debris-covered and clean-ice sites combine to create we observe~~ a melt-enhancing effect ~~that becomes particularly potent during monsoon : the~~ during monsoon conditions. The dark debris surface absorbs almost 90% of $SW_\downarrow$ in the case of Hailuogou ~~. With~~ (Table A2), and with a short conduction length ($1\,cm$), the energy influx ~~leads almost directly~~ goes almost entirely to melt. ~~The cold surface favours condensation and a strong temperature gradient between the surface and the air (g_T pre-monsoon: −2.08, monsoon: −2.61 $°C\,m^{-1}$). Driven~~
670 ~~by~~ Shortwave fluxes reduce during the monsoon, yet melt nonetheless increases, as higher wind speeds ~~(Table A3, Figures 7 and A9)and moist air during monsoon, both turbulent fluxes (H and LE)thus become potent~~ enhance turbulence resulting in an increase in H (Section 4.5 and Table A3). Warmer and more humid air increases LE inputs from condensation at the cold surface (Table A3 and Figure A9). Both turbulent fluxes thus become important sources of melt energy (Section 4.4.3). This adds ~~detail~~ detailed insights to prior observations and modelling ~~results, that thin debris~~ inferences that debris
675 around or below the critical thickness causes higher melt rates than at both clean-ice sites and sites with thicker debris cover ~~(Reznichenko et al., 2010; Östrem, 1959; Reid and Brock, 2010; Fyffe et al., 2020), especially in humid environments (Evatt et al., 2015), e. g. the location of Hailuogou glacier.~~

5.4 ~~Sensitivity of seasonal flux changes to elevation and debris thickness~~

~~Our results are derived from simulations at one location (AWS) on each glacier. To understand how representative they are of~~
680 ~~conditions across the glacier ablation zone at each site, and across the possible range of debris thicknesses in particular, we conduct a sensitivity experiment at each site. We re-run the model synthetically varying the AWS elevation to represent the range of elevation of each glacier ablation zone by applying a T_a lapse rate of $0.6\,°C/100m$ and, for the~~ (Östrem, 1959; ?; Reznichenko et al . Artificially applying thick debris to Hailuogou, while acknowledging the limitations of this experiment (Section A1), results in the same change pattern as the one observed on the other debris-covered ~~sites, by varying also the debris thickness in the~~
685 ~~range 10-80 cm (for ranges and steps see Table A1). Using the station-measured, accumulated albedo is not appropriate during this experiment, due to changing snow conditions with varying elevation. We therefore include the parameterisation introduced by Ding et al. (2017) for modelling α. From the resulting range of EB flux outputs, we calculate the range of expected changes for the entire ablation zone when moving from pre-monsoon to monsoon (Δ-range). This allows us to place our results in the context of the changes that can be expected over the entire ablation zone, given its elevation span and debris thickness~~
690 ~~variability. Figure A12 shows that even accounting for the range of conditions across each glacier ablation area, the pattern of pre-monsoon to monsoon difference in flux components, and importantly dQ, remain similar for debris-covered sites: The Δ-range of dQ stays within the uncertainty range, with the exception of Langtang, where the unrealistic combination of relatively thin debris and low elevation causes high dQ Δ-range. This lends confidence to the results obtained at the individual AWS locations. Although we adjusted forcing data for elevation in this exercise, we could not represent the effects of variable~~

	SW↓	SW↑	LW↓	LW↑	LE	H	G	M
LIR	▼	▲	▼	▲<	▲	▲	◼<	◼<
LAN	▼	▲	▼	▲	▲	▲	◼<	◼<
CNU	▼	▲	▼	▲<	▲<	▲	◼<	◼<
24K	▼	▲	▼	▲<	▲<	▲	◼<	◼<
YAL	▼	▲	▼	▲	▼ switched	▲ switched	◼	◼<
NO4	▼	▲	▼	▲	▼ switched	▼	◼	◼
HAI	▼	▲	▼	▲<	▼	▼	◼	◼

Legend:
- ▼ incoming flux
- ▲ outgoing flux
- ◼ increasing value
- ◼ decreasing value
- < change small/within uncertainty range
- ⧖ switched sign

Figure 8. Symbolic representation of changes in energy balance components from pre-monsoon to monsoon. Triangles pointing down/up indicate a positive/negative flux with regards to our sign-convention, where positive/negative means a flux towards/away from the surface. Red/blue indicate an increasing/decreasing value of the flux when moving from pre-monsoon to monsoon. When signs switch, the underlying, empty triangles indicate the pre-monsoonal direction of the flux, while the overlying, colored ones indicate the monsoonal flux

695 ~~debris thicknesses in modifying $2\,m$ meteorological variables (Steiner and Pellicciotti, 2016; Shaw et al., 2016). This comes with the assumption that surface-atmosphere interactions are negligible compared to the altitudinal patterns and temporal changes. While this might be acceptable at thicker debris sites, it is more questionable at Hailuogou, where the observations were taken above thin and cold debris. However, also at this site, the Δ-range ends up to be small ($5\,W\,m^{-2}$) and close to zero when debris between 10 and $80\,cm$ thickness is applied artificially.~~ glaciers: Melt rates remain almost unchanged when going

700 from pre-monsoon to monsoon (Section A1).

~~Ranges of elevations and debris thicknesses used for the sensitivity runs, including the glacier terminus elevation (min), the AWS elevation (AWS) and the upper debris limit on debris-covered glaciers or to the approximated ELA elevation on clean-ice glaciers (max). We also show the range of debris thicknesses h_m modelled for debris-covered glacier sites. All combinations of elevations and debris thicknesses were used. **Glacier Lirung Langtang Yala Changri Nup 24K Parlung No.4 Hailuogou**~~

705 ~~**min** [$m.asl$] 3990 4500 5170 5270 3910 4620 2980 **AWS** [$m.asl$] 4076 4557 5350 5471 3900 4800 3550 **max** [$m.asl$] 4400 5600 5400 5600 4200 5400 3700~~

5.4 ~~**Limitations**~~

~~Our modelling approach allowed us to constrain the energy and mass balance at the AWS location in the best possible way for the different glacier surface types. Two debris-specific parameters (k_d and z_0) were optimised in two separate steps at the debris sites (see section 3.3) and α was derived from measured $SW_\downarrow$ and $SW_\uparrow$ and given as an input at all sites. While this is not a feasible approach at the scale of entire glaciers, for application at other sites, or for future simulations, as it requires specific observations of radiation and ablation, both choices were made here in order to constrain the energy balance with observations to the greatest degree possible. Requisite data (e.g. thermistor strings, wind towers, high-resolution topography) to estimate these two parameters with established methods were not uniformly available across our study sites. These observational methods themselves can be sensitive to the measurement period (e.g. Nicholson and Benn, 2006) and are subject of ongoing research (e.g. Rounce et al., 2015; Miles et al., 2017; Rowan et al., 2020; Quincey et al., 2017), so we concluded that the calibration approach here was best suited to the application at all sites. In this respect, all optimized values fall within the expected range based on prior energy-balance studies on debris-covered glaciers (Yang et al., 2017; Rounce et al., 2015; Evat , but consistent measurements of debris parameters remain a community research priority to ensure robust modelling of sub-debris melt. To represent evaporation and the latent heat flux from the debris, we assigned an interception storage of $2\,mm$ water to the debris surface, as, to the authors' knowledge, very few measurements have been collected of the debris layer's interception capacity and moisture content. This is important because the thermal properties of debris vary with moisture fluctuations inside the debris (Nicholson and Benn, 2006; Collier et al., 2014; Steiner et al., 2018), so the moisture retention properties of the surface debris layer may play an important role in regulating energy transfer. However, these thermal properties have been found to be stable during the core monsoon months (Rowan et al., 2020), so we kept k_d constant in time at each site in our model. Additional, targeted investigations should examine the possible role of water storage and mobility within debris layers (Giese et al., 2020; Collier et al., 2014).~~

5.4 Implications for Himalayan glaciers in a changing climate

~~Our results show that the surface type plays a large role in modulating a glaciers' response in the seasonal transition from premonsoon to monsoon: we find a melt-enhancing effect of thin debris, driven by enhanced energy uptake attributable to low albedo and turbulent energy fluxes. We also find that, on clean-ice glaciers, LE switches seasonally to become a source instead of a sink of energy to the surface, while net radiation determines melt. Importantly, we additionally identify a melt-equalizing effect of debris cover under monsoon conditions at a number of sites.~~ Monsoon-influenced, summer-accumulation glaciers (such as Langtang, Lirung, Yala, and Changri Nup) have been previously shown to be especially vulnerable to warming due to a decrease in accumulation and an enhancement of ablation ~~with lowering~~ due to reduced albedo (Fujita and Ageta, 2000), and our results confirm that ~~net shortwave radiation~~ SW_{net} is the key control on monsoon-period melt rates for ~~clean ice glaciers~~ clean-ice glaciers (Section 4.4.1). Our results also emphasize that the longevity of pre-monsoon snowcover into the monsoon period is a key control on melt rates (Section 4.1), supporting past findings that the strength and timing of the monsoon onset has a profound impact on small mountain glaciers (Mölg et al., 2014, 2012) through the phase change of precipitation in the transition to monsoon conditions (Fujita and Ageta, 2000; Ding et al., 2017; Zhu et al., 2018). ~~The distinct responses of the surface energy balance of debris-covered and clean-ice glaciers to the pre-monsoon to monsoon transition potentially~~

~~accumulate to large mass balance biases when not adequately taken into account in models. It is thus important to also consider how this seasonal transition may evolve under changing climate, and what the consequences for glacier mass balance might be. All future model simulations~~ Importantly, our insights into the differential response of glaciers with different surface types to the monsoon and its onset offers keys to interpret their future response under a changing climate:

All future climate scenarios agree on continued warming during the 21st century over High Mountain Asia (?), together with a strengthening of elevation dependent warming (Palazzi et al., 2017) and increases in moisture availability (?). An analysis on the ensemble estimates of regionally downscaled CMIP5 projections (CORDEX) for the Himalayas (Sanjay et al., 2017) shows that total summer precipitation is projected to increase for 2036-2065 (2066-2095) by 4.4% (10.5%) in the Central Himalaya and by 6.8% (10.4%) in the Eastern Himalaya under RCP4.5 scenarios, relative to 1976-2005. While there is broad model consensus on the increase in future precipitation, there is little consensus on the future variability, frequency and spatial distribution of precipitation across High Mountain Asia (Kadel et al., 2018; Sanjay et al., 2017)~~, which is likely a result of complex and poorly understood drivers of past monsoon changes (Saha et al., 2014; Saha and Ghosh, 2019), coarse resolution of the baseline products and topographic variability in the region (Sanjay et al., 2017)~~. A slight shift towards an earlier monsoon onset of <5 days over the coming century together with an increasing shift towards a later retreat by 5 to 10 days (mid-century) and 10 to 15 days (end-century) might increase the length of the monsoon period, with stronger lengthening in the Eastern Himalaya (Moon and Ha, 2020).

The prospect of warmer temperatures together with increased precipitation would (1) cause a shift in the precipitation partition from snow to rain in the monsoon, resulting in snow cover shifting to higher elevations and increasing total melt; (2) potentially lead to an increase in early spring snowfall, which would delay the onset of ice melt; (3) increase the likelihood of ephemeral monsoonal snow cover but move it to higher elevations, thus leaving more of the lower ablation zones exposed; (4) increase the ~~wetbulb~~ wet-bulb temperature together with humidity to result in a further reduction of the solid fraction of precipitation during monsoon. Overall it is likely that glacier ablation zones will be exposed for longer periods under future climate due to a net decrease of the snow covered duration, with a resulting increase in total ablation. A lengthening of the monsoon into autumn, on the other hand, (Moon and Ha, 2020) would somewhat offset warmer air temperatures with regards to the late-season melt for all glacier types.

~~Warmer~~ The expected warmer and wetter monsoonal conditions, including increased cloudiness, are likely to result in an overall increase of melt rates on clean-ice and ~~dirty-ice glaciers~~ glaciers with debris cover around or below the critical thickness. This is because (1) they are more directly controlled by R_{net}net radiation (comprising all short- and long-wave fluxes), which is likely to increase in magnitude (Section 4.4.1); (2) the turbulent fluxes towards cold surfaces are also likely to increase in magnitude, and they tend to 'work against' these types of glaciers (Section 4.4.1 and 4.4.3). In contrast, the turbulent fluxes 'work for' ~~debris-covered glaciers~~ the glaciers with debris above the critical thickness, and the melt-equalizing effect of debris under monsoon (Section 4.4.2) would likely remain in place . With these components summing up to have an overall protective effect on ~~debris-covered glaciers~~ glaciers with thick debris, they are likely to resist the projected changes in the monsoonal summer longer into the future. Previous studies suggested that the mass balance of ~~DCGs~~ debris-covered glaciers might be less sensitive to climate warming than clean-ice glaciers (e.g. Anderson and Mackintosh, 2012; Wijngaard et al., 2019; Mattson,

2000). Here we confirm this hypothesis and suggest that this is ~~even more the case~~ particularly so under monsoonal conditions. ~~Simplified methods of glacier melt calculation (e.g. relying only on temperature or temperature and shortwave radiation) may integrate some of these processes through calibration (e.g. Ragettli et al., 2016). However, in a study on two clean-ice glaciers (Yala and Mera), Litt et al. (2019) were able to transfer Temperature Index and Enhanced Temperature Index models between sites and years only during pre-monsoon. During monsoon, the transfer failed due to site-specific and inter-annually variable cloudiness.~~

5.5 ~~Future work~~

~~By modelling seven different study glaciers across the Himalayan arc, we have been able to identify important monsoon effects on the energy and mass balance of debris-covered and~~ We also suggest that glaciers with debris under the critical thickness might be even more sensitive to future monsoons than clean-ice ~~glaciers. In the context of the large spatial and inter-annual variability in the climate, including the monsoon strength and timing, our sample size remains small due to data availability. The timing and quantity of spring snow-cover and monsoonal snowfalls have large effects on the energy and mass balance, and these variables can be highly variable between years. A future analysis could leverage a greater number of complete AWS records, and possibly multi-year records, in order to extend some of our findings. Despite the advanced representation in Tethys-Chloris, the surfaces of glaciers, and especially of debris-covered glaciers, are more complex systems than indicated at the AWS location. Future work should be invested into spatially distributing forcing data and parameters necessary to run energy-balance models in a distributed framework at glacier and catchment scales. Studies employing distributed energy balance models could, for example, test the melt-equalizing effect of debris at the glacier scale and its overall effect on the catchment runoff. This could be combined with generating spatially consistent forcing data using high-resolution weather modelling as in Bonekamp et al. (2019) or Potter et al. (2020), and expanded to larger domains. Realistic representations of the glacier surface, including distributed debris thickness, and supraglacial features, such as ice cliffs and surface ponds, should also be established to provide well-constrained water budgets and improved representations of glacierised environments in land-surface models under present and future environmental conditions.~~glaciers.

6   Conclusions

~~By modelling~~ We model the energy and mass balance of seven glaciers in the ~~Himalayas at~~ Central and Eastern Himalaya at seven on-glacier weather stations~~, we identify and explain the main effects on the energy and mass balance caused by the Indian and East Asian summer monsoons. Heavy cloud cover, liquid precipitation, wind speed, the presence and thickness of debris cover, and elevation shape the energy and mass balances of the Himalayan glaciers~~. We find that:

1. At all sites, the largest mass loss component during the ablation season ~~. The timing of snow melt-out and~~ is ice melt, followed by snowmelt and sublimation, while the last only plays a role at our highest sites and outside of the core monsoon. We find that the seasonal energy and mass balance is strongly controlled by variations of absorbed shortwave

33

radiation, a result of the prevalence of spring snow cover and the ~~presence of ephemeral monsoonal snowcover play a particularly important role , especially at high elevations. We highlight key pre-monsoon to monsoon changes in energy fluxes, distinct for clean-ice and debris-covered glacier sites: the melt of clean-ice glaciers is primarily radiation-driven at any point during the ablation season, and strongly influenced by albedo variations . The latent heat flux can initially be a small sink and turn into a source during the core monsoon. Debris cover can act in two ways: (1) Once a debris layer of a few centimetres is established, it~~ occurence of ephemeral monsoonal snow accumulation.

2. Debris cover above the critical thickness returns most of the ~~heat~~ energy it absorbs back to the atmosphere via long-wave emission and turbulent heat fluxes. ~~The sensible heat flux reduces during core monsoon, but the latent heat flux removes energy from the surface due to evaporation~~ While H is primarily controlled by the temperature gradient between surface and air, LE is controlled by the availability of liquid water ~~. The turbulent fluxes readjust in this way to monsoonal temperature, wind and moisture regimes, maintaining a nearly constant melt rate over the entire ablation period. Sensitivity analyses of our energy-balance model shows that these findings hold for large portions of the debris-covered glacier surfaces. (2) When it is thin, debris amplifies the incoming energy due to its dark and cold surface , small conduction distance to the ice and sensitivity to turbulence. The~~ at the debris surface. When debris is around or under the critical thickness, the melt is more directly radiation-driven. In this case, however, melt is additionally modulated by the turbulent fluxes H and LE, for which wind speed is the primary control, and the cold surface favours condensation rather than evaporation.

3. The response of the glacier mass and energy balance to the monsoon depends on the surface type: melt-rates increase compared to the pre-monsoon at the clean-ice glaciers and the glaciers with thin debris cover, while they stay similar at the glaciers with thick debris cover. We attribute these differences to the role the turbulent fluxes play for each surface type. At the glaciers with thick debris cover, where the turbulent fluxes 'work for' the glacier, evaporation of the additionally available moisture (LE) provides extra cooling during the monsoon. The evaporation of liquid water is a moisture limited process during the pre-monsoon and turns into an energy-limited process during the monsoon. The cooling induced by H at the same time decreases, with the result of unchanged available melt-energy M during monsoon. In a sensitivity experiment, we confirm that these results are representative of the entire ablation zones of the thickly debris-covered glaciers~~by returning absorbed energy to the atmosphere, and tend to~~ . At the clean-ice sites, in contrast, the melt is mostly radiation controlled throughout the ablation season and varies greatly over the elevation profile of the ablation zone. The turbulent fluxes play a subordinate role there, but can switch from melt-reducing to melt-enhancing in the seasonal transition into the monsoon. At the thin debris-covered site, on the other hand, the turbulent fluxes always 'work against' ~~clean-ice and dirty-ice glaciers under monsoonal conditions. We thus~~ the glacier and intensify during the monsoon.

Given these findings, under projected future monsoonal conditions, namely warmer and possibly longer and wetter monsoons (Sanjay et al., 2017; Moon and Ha, 2020; **?**), we expect the mass balance of ~~debris-covered glaciers~~ glaciers

with thick debris-cover to react less sensitively ~~to projected future monsoon changes~~ than clean-ice ~~and dirty-ice glaciers~~ ~~.~~ glaciers and glaciers with thin debris cover.

36

Appendix A: Climatic and meteorological conditions

Average mean monthly 2 m air temperatures have a similar pattern at all study sites (Figure A1a), with a slow increase from January to a peak between July and August, just after peak monsoon, and a steeper decline from post-monsoon into winter. Incoming shortwave radiation (Figure A1b) shows a clear peak before monsoon onset at all sites. A smaller secondary peak is reached just after the monsoon in October at the Central Himalayan sites, but not at the Eastern Himalayan sites. Interruptions in monsoonal overcast conditions (break periods) seem to be more common at the eastern sites, leading to occasional secondary peaks in incoming shortwave radiation during monsoon. $LW_{\downarrow}$ follows a similar regime as Ta, with highest values reached during the core monsoon (Figure A1c). The yearly cycle of wind speeds (Figure A1d) varies considerably between sites. Common characteristics for most sites (except for Changri Nup) are that wind speeds are highest around December/January and that monsoonal wind speeds are generally higher than during the shoulder seasons. There is a clear difference in the seasonal evolution of precipitation between the Central (Lirung, Lantang, Yala, Changri Nup) and the Eastern Himalayan sites (24K, Parlung No.4, Hailuogou) (Figure A1e): relatively high mean monthly precipitation during the monsoon period is contrasted by comparably low precipitation outside of this period. The eastern sites have less pronounced monsoonal precipitation peaks, and more gradual changes in precipitation intensities over the annual cycle. The Parlung sites (24K and Parlung No.4) have two precipitation peaks: during spring and monsoon. Hailuogou exhibits the smoothest evolution over the annual cycle with a clear maximum in July. A simple monsoon index (MI) is calculated for each year including the study year as the ratio between monsoon precipitation and annual average precipitation (Figure A1e). This value tends to be higher in the Central Himalaya compared to the sites on the South-Eastern Tibetan Plateau.

At each site, we define the onset and recession date of monsoon based on visual inspection of the AWS records, observing the seasonal shift of air temperature, relative humidity, and longwave and shortwave radiation. For this, we define the date after which clear shifts are observable in the variables' regime (Figures A3 to A9).

Predictive power of temperature gradient between surface and air (gT) and wind speed (Ws) and their combination for determining H and LE. 'All' indicates a multiple polynomial regression model using both variables, otherwise a univariate polynomial regression model was used, and both models had 2 degrees of freedom.
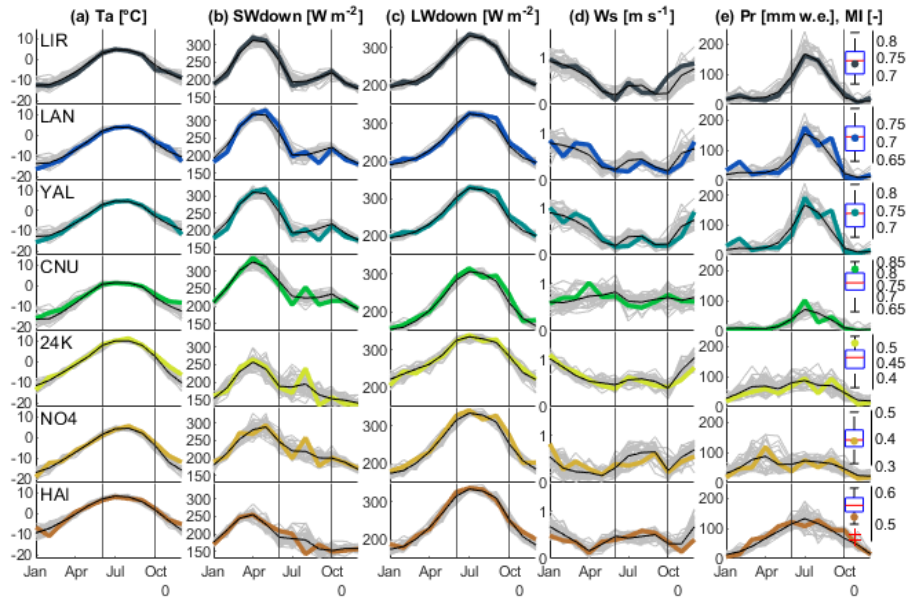
37

Figure A1. Monthly climatology derived from ERA5-Land for 1981-2019 (grey background lines), along with the monthly averages (black lines) and the study year at each glacier (colored lines). Plotted meteorological variables are **(a)** mean air temperature (Ta), **(b)** incoming shortwave radiation ($SW_\downarrow$), **(c)** incoming longwave radiation ($LW_\downarrow$), **(d)** wind speed (Ws) and **(e)** monthly precipitation sums (Pr). Black vertical lines indicate the average region-wide monsoon season. Boxplots show the monsoon index (MI) over ERA5-Land period as the fraction of monsoonal (June-September) to annual precipitation, with the colored dot indicating the value for the study year.
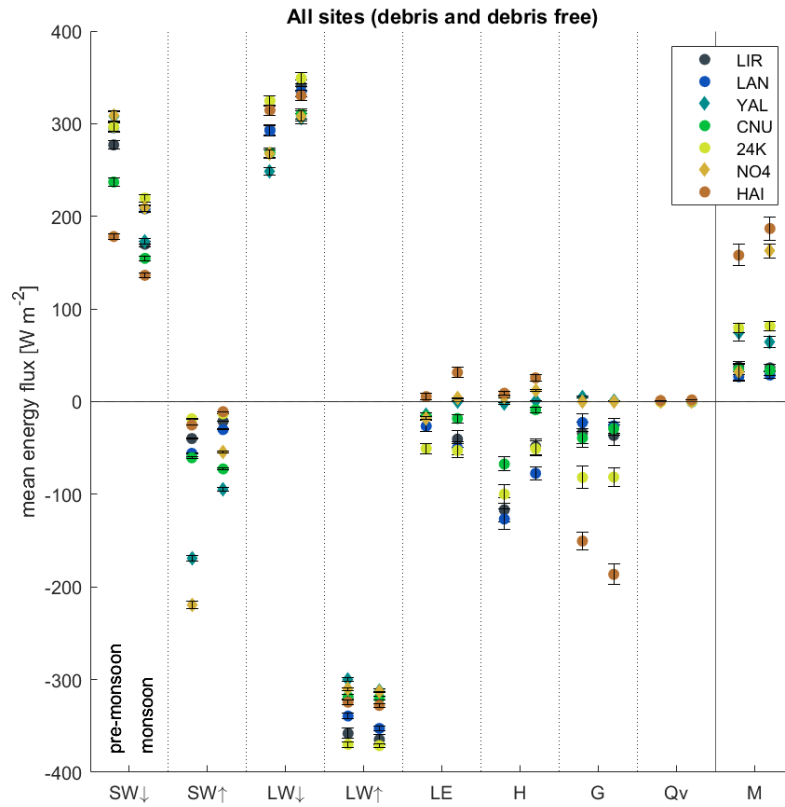
Figure A2. All energy balance components of all glaciers in comparison, split into pre-monsoon and monsoon; black bars indicate the uncertainty range;
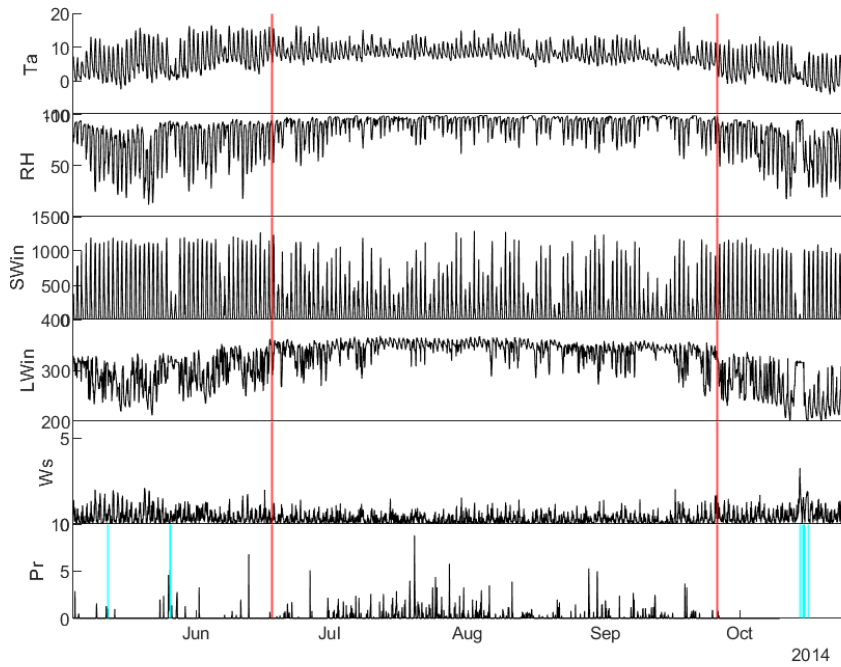
Figure A3. Meteoroligical observations on Lirung during the ablation season recorded by AWS; Red vertical lines indicate monsoon onset and end; ~~Blue~~ cyan indicates time steps with snow cover at the AWS location, as determined from α (>0.5)

Figure A4. Meteoroligical observations on Langtang during the ablation season recorded by AWS; Red vertical lines indicate monsoon onset and end; ~~Blue~~ cyan indicates time steps with snow cover at the AWS location, as determined from α (>0.5)

Figure A5. Meteoroligical observations on Yala during the ablation season recorded by AWS; Red vertical lines indicate monsoon onset and end; ~~Blue~~ cyan indicates time steps with snow cover at the AWS location, as determined from α (>0.5)
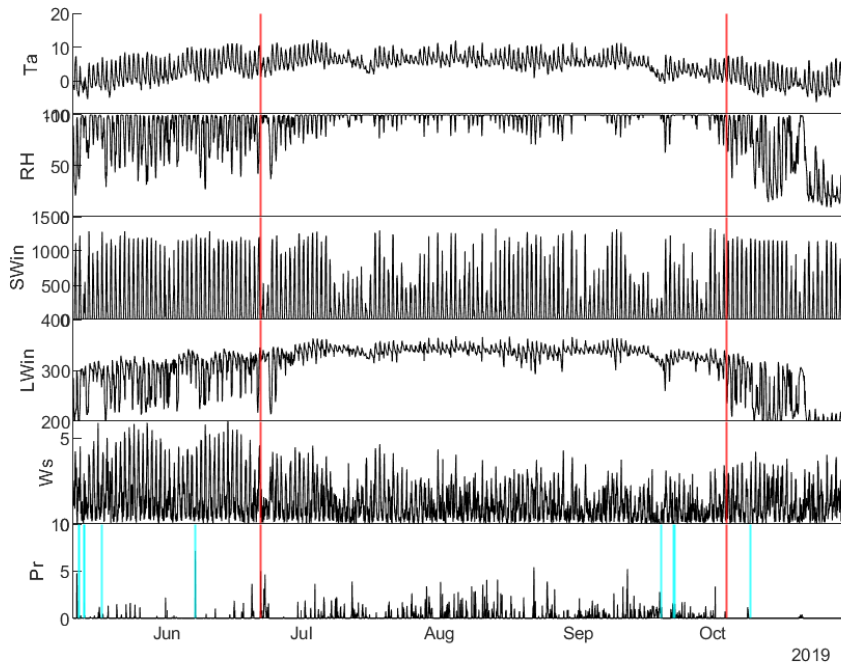
Figure A6. Meteoroligical observations on Changri Nup during the ablation season recorded by AWS; Red vertical lines indicate monsoon onset and end; Blue cyan indicates time steps with snow cover at the AWS location, as determined from α (>0.5)
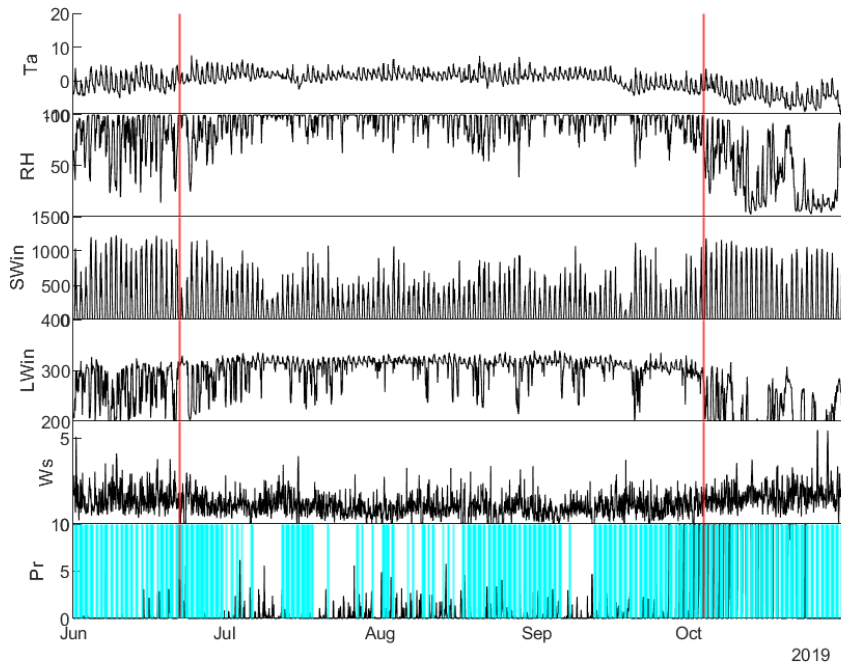
43
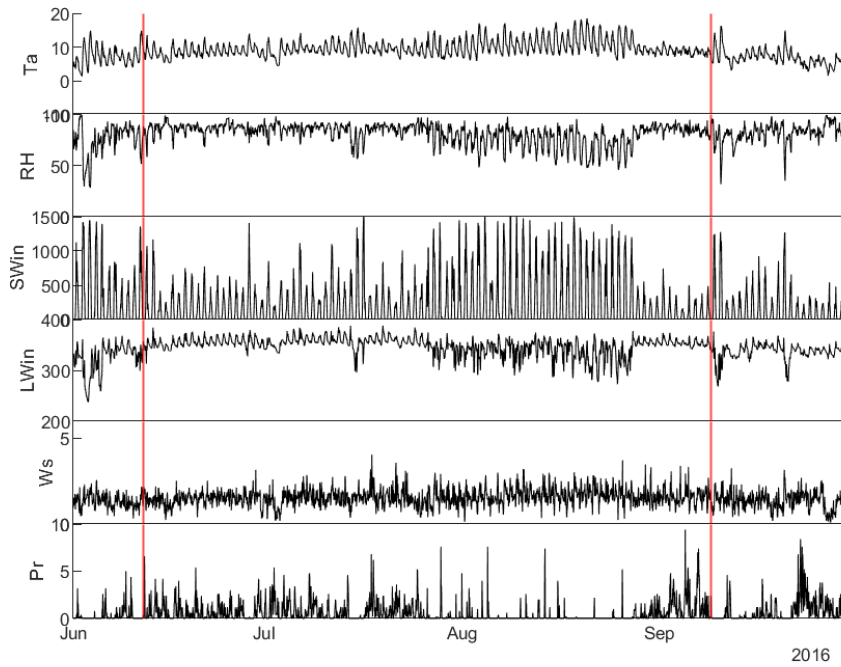
Figure A7. Meteoroligical observations on 24K during the ablation season recorded by AWS; Red vertical lines indicate monsoon onset and end; ~~Blue~~ cyan indicates time steps with snow cover at the AWS location, as determined from α (>0.5)

Figure A8. Meteoroligical observations on Parlung No.4 during the ablation season recorded by AWS; Red vertical lines indicate monsoon onset and end; ~~Blue~~ cyan indicates time steps with snow cover at the AWS location, as determined from α (>0.5)
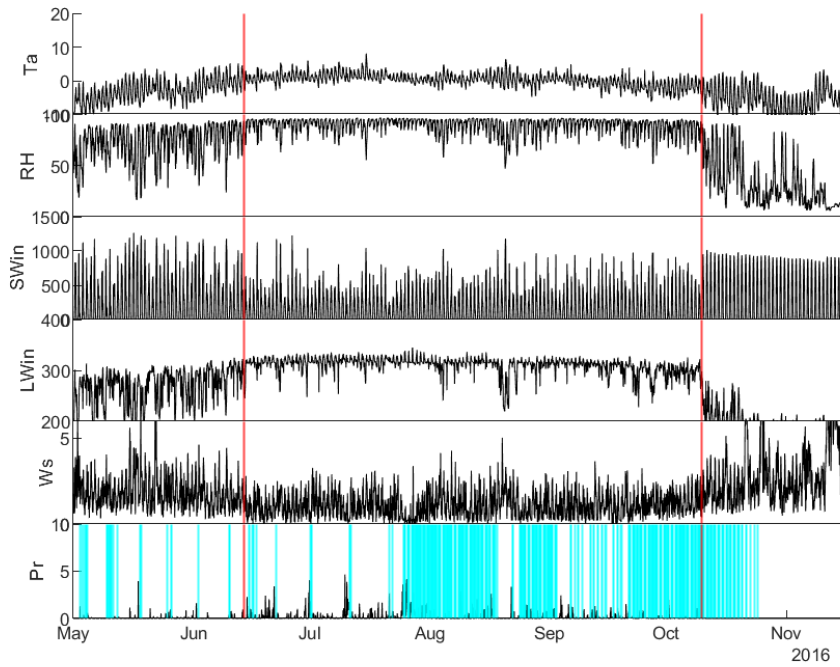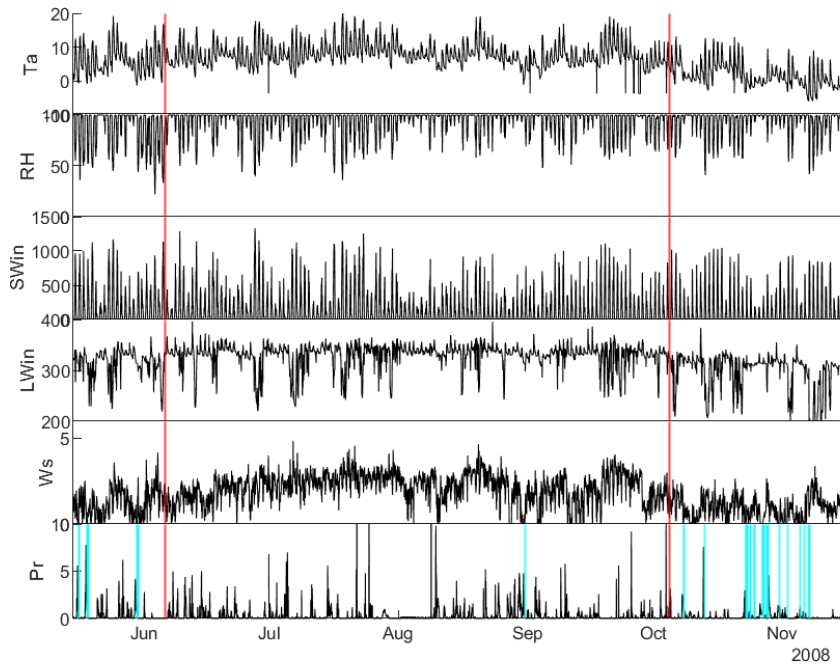
Figure A9. Meteoroligical observations on Hailuogou during the ablation season recorded by AWS; Red vertical lines indicate monsoon onset and end; ~~Blue~~ cyan indicates time steps with snow cover at the AWS location, as determined from α (>0.5)
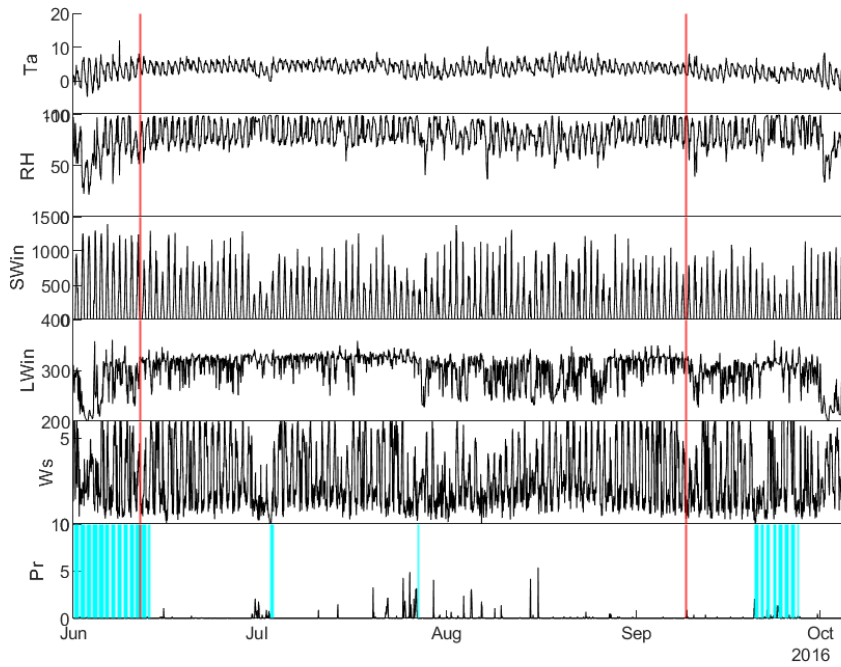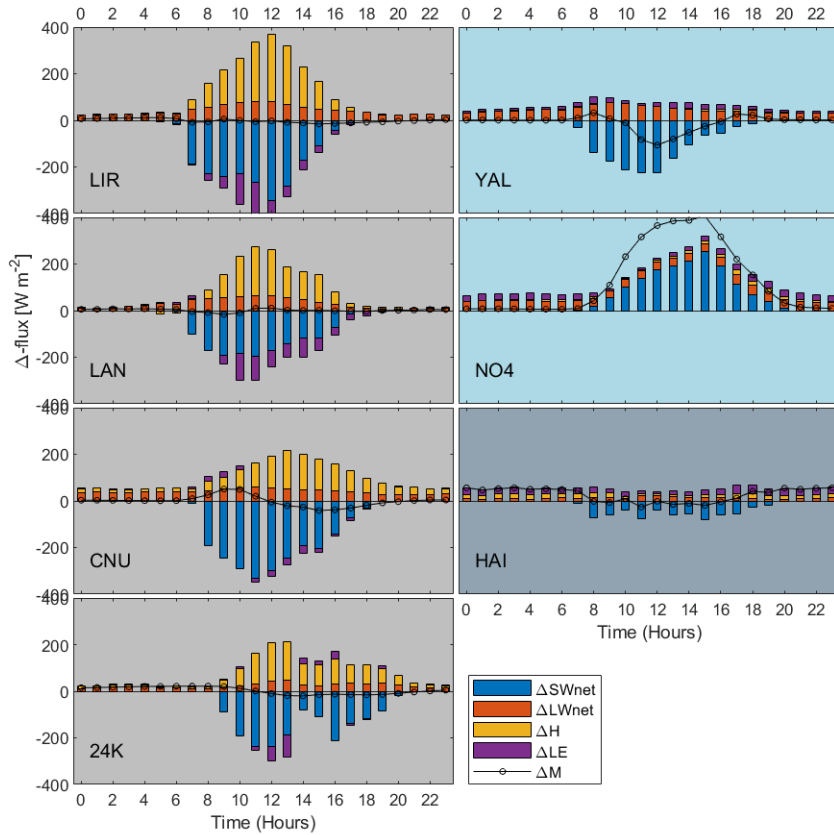
Figure A11. Energy flux differences in the diurnal cycle (stacked) between pre-monsoon and monsoon; The direction of change is to be considered relative to the sign of the orginial flux. ~~Fluxes towards/away from the surface have a positive/~~Positive and negative sign ~~. For example, a positive change in a negative flux means a reduction in~~ corresponds to energy added or removed from the ~~magnitude flux~~glacier, ~~and can also lead to a change in sign.~~ respectively; Grey background indicates ~~debris covered~~ debris-covered site~~;~~, light blue indicates clean ice sites ~~; grey-blue~~ and gray-blue indicates 1cm debris site

47
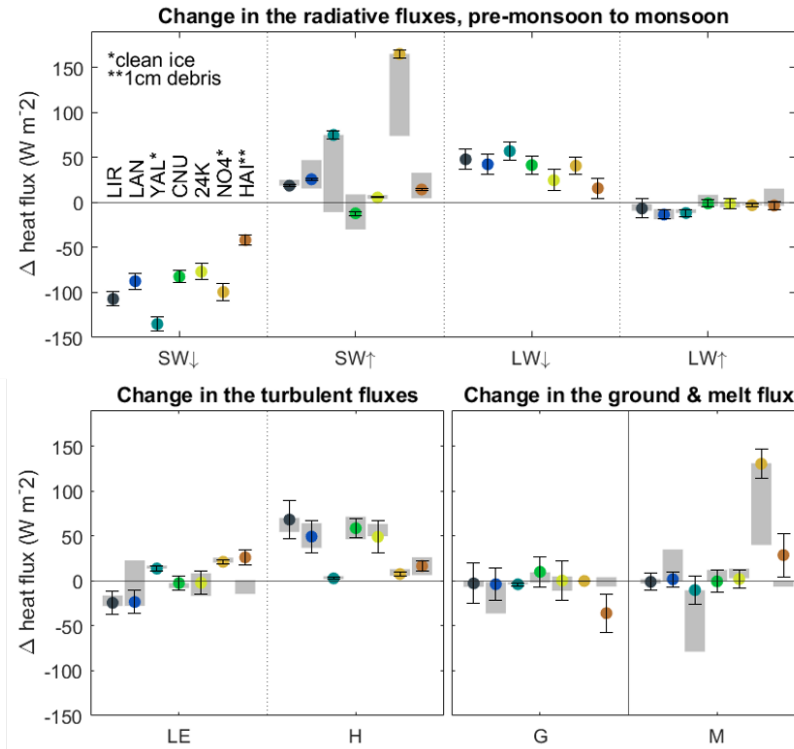
Figure A12. Changes in the individual fluxes when moving from premonsoon to monsoon. Color dots indicate 'standard' runs with AWS site specific conditions. Black bars indicate the uncertainty range on the standard runs. Grey indicates the sensitivity of flux changes (Δ-range) to debris thickness varied from 10 and 80 cm combined with the elevation range of debris-covered ablation zone of the individual glaciers; Positive and negative sign corresponds to energy added or removed from the glacier, respectively;

A1 Sensitivity of seasonal flux changes to elevation and debris thickness

Our results are derived from simulations at one location (AWS) on each glacier. To understand how representative they are of conditions across the glacier ablation zone at each site, and across the possible range of debris thicknesses in particular, we conduct a sensitivity experiment at each site. We assume that the strongest changes in meteorological forcing with elevation would be the Ta, which in turns controls the precipitation partition and the albedo. We re-run the model synthetically varying the AWS elevation to represent the range of elevation of each glacier ablation zone by applying a T_a lapse rate of $0.6\,°C/100m$ and, for the debris-covered sites, by varying also the debris thickness in the range 10-80 cm (for ranges and steps see Table A1). Using the station-measured, accumulated albedo is not appropriate during this experiment, due to changing snow conditions with varying elevation. We therefore include the parameterisation introduced by Ding et al. (2017) for modelling α. From the resulting range of EB flux outputs, we calculate the range of expected changes for the entire ablation zone when moving from pre-monsoon to monsoon (Δ-range). This allows us to place our results in the context of the changes that can be expected over the entire ablation zone, given its elevation span and debris thickness variability. Figure A12 shows that even accounting for the range of conditions across each glacier ablation area, the pattern of pre-monsoon to monsoon difference in flux components, and importantly M, remain similar for debris-covered sites: The Δ-range of M stays within the uncertainty range, with the exception of Langtang, where the unrealistic combination of relatively thin debris and low elevation causes high M Δ-range. This lends confidence to the results obtained at the individual AWS locations. Although we adjusted forcing data for elevation in this exercise, we could not represent the effects of variable debris thicknesses in modifying $2m$ meteorological variables (Steiner and Pellicciotti, 2016; Shaw et al., 2016). This comes with the assumption that surface-atmosphere interactions are negligible compared to the altitudinal patterns and temporal changes. While this might be acceptable at thicker debris sites, it is more questionable at Hailuogou, where the observations were taken above thin and cold debris. However, also at this site, the Δ-range ends up to be small ($5\,W\,m^{-2}$) and close to zero when debris between 10 and $80\,cm$ thickness is applied artificially.

Table A1. Ranges of elevations and debris thicknesses used for the sensitivity runs, including the glacier terminus elevation (min), the AWS elevation (AWS) and the upper debris limit on debris-covered glaciers or to the approximated ELA elevation on clean-ice glaciers (max). We also show the range of debris thicknesses h_m modelled for debris-covered glacier sites. All combinations of elevations and debris thicknesses were used.

Glacier		Lirung	Langtang	Yala	Changri Nup	24K	Parlung No.4	Hailuogou
min	$[m.asl]$	3990	4500	5170	5270	3910	4620	2980
AWS	$[m.asl]$	4076	4557	5350	5471	3900	4800	3550
max	$[m.asl]$	4400	5600	5400	5600	4200	5400	3700
h_d $[cm]$	10, 20, 30, 40, 50, 60, 70, 80							

Table A2. Mean energy balance components at each site and for pre-monsoon (pre), monsoon (mon), and post-monsoon (post) periods, as well as flux magnitude changes from pre-monsoon to monsoon, and monsoon to post-monsoon. All values are in $W\,m^{-2}$.

fluxes in W/m2		SW↓ pre	SW↓ mon	SW↓ post	SW↑ pre	SW↑ mon	SW↑ post	LW↓ pre	LW↓ mon	LW↓ post	LW↑ pre	LW↑ mon	LW↑ post	LE pre	LE mon	LE post
LIR	mean	277.1	170.0	224.1	-39.8	-21.1	-41.3	293.3	341.2	264.0	-358.1	-364.8	-340.4	-16.0	-40.4	-1.9
	Δ		-107.1	54.1		18.7	-20.2		47.9	-77.2		-6.7	24.4		-24.4	38.5
LAN	mean	295.6	208.1	262.4	-55.9	-30.1	-48.6	292.3	334.7	238.6	-339.3	-352.8	-326.1	-26.4	-49.9	-5.8
	Δ		-87.5	54.3		25.7	-18.4		42.3	-96.0		-13.5	26.7		-23.5	44.1
YAL	mean	307.7	172.7	271.8	-169.4	-94.4	-195.0	248.5	305.5	212.3	-299.8	-311.6	-287.1	-13.7	0.1	-12.2
	Δ		-135.0	99.1		75.0	-100.6		57.0	-93.2		-11.7	24.4		13.7	-12.3
CNU	mean	237.1	154.7	258.1	-60.6	-72.7	-126.0	268.8	310.2	196.4	-318.7	-319.7	-300.4	-15.7	-18.1	-3.1
	Δ		-82.4	103.4		-12.1	-53.3		41.5	-113.8		-1.0	19.3		-2.5	15.0
24K	mean	296.6	219.7	140.9	-18.5	-13.0	-8.3	324.6	349.3	336.6	-369.9	-371.3	-351.0	-50.6	-52.7	-40.0
	Δ		-76.9	-78.8		5.4	4.7		24.7	-12.7		-1.3	20.3		-2.1	12.7
NO4	mean	308.5	209.1	197.3	-219.6	-54.8	-81.5	267.5	308.2	261.5	-310.3	-313.4	-310.5	-17.6	3.6	-18.5
	Δ		-99.5	-11.8		164.8	-26.7		40.7	-46.7		-3.1	2.9		21.2	-22.1
HAI	mean	178.2	136.4	105.8	-25.2	-10.8	-28.4	314.6	330.3	273.1	-324.5	-327.9	-309.1	5.4	31.6	-4.8
	Δ		-41.8	-30.6		14.4	-17.6		15.7	-57.2		-3.4	18.8		26.2	-36.4

fluxes in W/m2		H pre	H mon	H post	Qv pre	Qv mon	Qv post	G pre	G mon	G post	dG pre	dG mon	dG post	M pre	M mon	M post
LIR	mean	-116.7	-48.4	-86.5	0.0	0.0	0.0	-33.7	-36.4	-18.7	5.6	0.0	16.6	37.5	36.5	19.0
	Δ		68.3	38.0		0.0	0.0		-2.7	-17.8		-5.6	-16.6		-1.0	17.5
LAN	mean	-126.7	-77.4	-111.4	0.0	-0.3	0.0	-22.5	-26.2	-7.8	2.2	0.0	27.3	26.9	28.7	10.4
	Δ		49.3	34.1		-0.3	-0.3		-3.7	-18.4		-2.2	-27.3		1.8	18.4
YAL	mean	-2.3	0.5	1.4	0.0	-0.2	-4.1	4.7	0.9	0.0	4.7	0.9	0.0	74.8	64.6	0.3
	Δ		2.8	-0.9		-0.2	3.9		-3.8	0.9		-3.8	0.9		-10.2	64.3
CNU	mean	-67.4	-8.7	-36.1	0.0	0.0	0.0	-39.2	-29.1	10.4	17.1	1.8	10.6	34.6	34.1	0.2
	Δ		58.7	27.4		0.0	0.0		10.1	-39.5		-15.3	-8.9		-0.5	33.9
24K	mean	-99.8	-50.8	-24.4	-0.3	0.2	0.6	-81.8	-81.4	-53.1	0.3	0.0	0.0	79.5	81.6	53.7
	Δ		49.0	-26.4		0.6	-0.4		0.4	-28.4		-0.3	0.0		2.1	27.9
NO4	mean	4.7	12.3	5.8	0.2	0.2	0.0	0.2	0.1	0.1	0.2	0.1	0.0	32.3	162.6	54.1
	Δ		7.6	6.6		0.0	0.2		-0.1	0.1		-0.1	0.1		130.4	108.5
HAI	mean	9.1	25.7	-9.9	1.2	1.9	0.1	-150.4	-186.4	-16.5	1.8	0.5	17.6	158.1	186.8	36.9
	Δ		16.6	35.5		0.7	1.8		-35.9	-169.9		-1.4	-17.2		28.7	149.9

Table A3. Mean cloud-cover fraction (ccf), relative humidity (RH), temperature gradient between surface and air (δ_T), wind speed (Ws) and the percentage of time during which the debris is modelled to hold intercepted water (In) for each site and season, also indicating percent changes between the sub-seasons.

		ccf [−]			RH [%]			δ_T [°C m⁻¹]			Ws [m s⁻¹]			In [%]		
		pre	mon	post	pre	mon	post	pre	mon	post	pre	mon	post	pre	mon	post
LIR	mean	0.76	0.91	0.74	68.1	90.8	67.1	1.19	0.78	0.89	0.47	0.27	0.52	40.1	74.0	26.4
	Δ		0.14	-0.16		22.6	-23.6		-0.40	0.10		-0.19	0.24		33.9	-47.6
LAN	mean	0.76	0.86	0.62	80.7	96.9	56.3	1.02	0.97	0.95	1.79	1.10	1.27	38.8	75.3	9.5
	Δ		0.10	-0.24		16.2	-40.6		-0.05	-0.02		-0.68	0.17		36.5	-65.8
YAL	mean	0.65	0.87	0.55	69.8	93.0	39.4	-0.36	-0.96	-0.89	1.74	1.00	1.68	-	-	-
	Δ		0.21	-0.32		23.2	-53.6		-0.59	0.07		-0.74	0.67		-	-
CNU	mean	0.78	0.89	0.58	71.2	89.2	39.3	1.69	0.25	0.89	1.88	1.09	2.48	16.2	79.3	5.3
	Δ		0.11	-0.31		18.1	-50.0		-1.44	0.64		-0.79	1.39		63.1	-74.0
24K	mean	0.70	0.82	0.91	73.1	80.6	81.2	1.86	0.73	0.18	1.33	1.56	1.35	56.8	79.1	84.3
	Δ		0.12	0.08		7.4	0.7		-1.13	-0.55		0.22	-0.21		22.3	5.2
NO4	mean	0.72	0.87	0.79	65.7	81.3	73.1	-0.78	-2.01	-0.62	2.96	2.67	3.23	-	-	-
	Δ		0.14	-0.07		15.7	-8.3		-1.22	1.39		-0.28	0.56		-	-
HAI	mean	0.88	0.93	0.91	81.3	92.3	90.6	-2.08	-2.61	0.38	1.23	2.15	0.93	99.8	100.0	75.6
	Δ		0.05	-0.01		10.9	-1.6		-0.53	2.99		0.91	-1.22		0.2	-24.4

References

Anderson, B. and Mackintosh, A.: Controls on mass balance sensitivity of maritime glaciers in the Southern Alps, New Zealand: the role of debris cover, Journal of Geophysical Research: Earth Surface, 117, 2012.

905 Azam, M., Wagnon, P., Vincent, C., Ramanathan, A., Favier, V., Mandal, A., and Pottakkal, J.: Processes governing the mass balance of Chhota Shigri Glacier (western Himalaya, India) assessed by point-scale surface energy balance measurements, Cryosphere, 8, 2195–2217, 2014.

Bélair, S., Crevier, L.-P., Mailhot, J., Bilodeau, B., and Delage, Y.: Operational implementation of the ISBA land surface scheme in the Canadian regional weather forecast model. Part I: Warm season results, Journal of hydrometeorology, 4, 352–370, 2003.

Bonekamp, P. N., de Kok, R. J., Collier, E., and Immerzeel, W. W.: Contrasting meteorological drivers of the glacier mass balance between 910 the Karakoram and central Himalaya, Frontiers in Earth Science, 7, 107, 2019.

Bookhagen, B. and Burbank, D. W.: Toward a complete Himalayan hydrological budget: Spatiotemporal distribution of snowmelt and rainfall and their impact on river discharge, Journal of Geophysical Research: Earth Surface, 115, 2010.

Botter, M., Zeeman, M., Burlando, P., and Fatichi, S.: Impacts of fertilization on grassland productivity and water quality across the European Alps: insights from a mechanistic model, Biogeosciences Discussions, pp. 1–35, 2020.

915 Brock, B. W., Willis, I. C., and Sharp, M. J.: Measurement and parameterization of albedo variations at Haut Glacier d'Arolla, Switzerland, Journal of Glaciology, 46, 675–688, 2000.

Brun, F., Berthier, E., Wagnon, P., Kääb, A., and Treichler, D.: A spatially resolved estimate of High Mountain Asia glacier mass balances from 2000 to 2016, Nature geoscience, 10, 668–673, 2017.

Collier, E. and Immerzeel, W. W.: High-resolution modeling of atmospheric dynamics in the Nepalese Himalaya, Journal of Geophysical 920 Research: Atmospheres, 120, 9882–9896, 2015.

Collier, E., Nicholson, L., Brock, B., Maussion, F., Essery, R., and Bush, A.: Representing moisture fluxes and phase changes in glacier debris cover using a reservoir approach, The Cryosphere, 8, 1429–1444, 2014.

Collier, E., Maussion, F., Nicholson, L., Mölg, T., Immerzeel, W., and Bush, A.: Impact of debris cover on glacier ablation and atmosphere-glacier feedbacks in the Karakoram, 2015.

925 Cuffey, K. M. and Paterson, W. S. B.: The physics of glaciers, Academic Press, 2010.

Ding, B., Yang, K., Qin, J., Wang, L., Chen, Y., and He, X.: The dependence of precipitation types on surface elevation and meteorological conditions and its parameterization, Journal of hydrology, 513, 154–163, 2014.

Ding, B., Yang, K., Yang, W., He, X., Chen, Y., Guo, X., Wang, L., Wu, H., and Yao, T.: Development of a Water and Enthalpy Budget-based Glacier mass balance Model (WEB-GM) and its preliminary validation, Water Resources Research, 53, 3146–3178, 2017.

930 Evatt, G. W., Abrahams, I. D., Heil, M., Mayer, C., Kingslake, J., Mitchell, S. L., Fowler, A. C., and Clark, C. D.: Glacial melt under a porous debris layer, Journal of Glaciology, 61, 825–836, 2015.

Farinotti, D., Huss, M., Fürst, J. J., Landmann, J., Machguth, H., Maussion, F., and Pandit, A.: A consensus estimate for the ice thickness distribution of all glaciers on Earth, Nature Geoscience, 12, 168–173, 2019.

Farinotti, D., Immerzeel, W. W., de Kok, R. J., Quincey, D. J., and Dehecq, A.: Manifestations and mechanisms of the Karakoram glacier 935 Anomaly, Nature Geoscience, 13, 8–16, 2020.

52

Fatichi, S., Ivanov, V. Y., and Caporali, E.: A mechanistic ecohydrological model to investigate complex interactions in cold and warm water-controlled environments: 1. Theoretical framework and plot-scale analysis, Journal of Advances in Modeling Earth Systems, 4, 2012.

Fujita, K Sakai, A. et al.: Modelling runoff from a Himalayan debris-covered glacier, Hydrol. Earth Syst. Sci, 18, 2679–2694, 2014.

940   Fujita, K. and Ageta, Y.: Effect of summer accumulation on glacier mass balance on the Tibetan Plateau revealed by mass-balance model, Journal of Glaciology, 46, 244–252, 2000.

Fujita, K., Takeuchi, N., and Seko, K.: Glaciological observations of Yala Glacier in Langtang Valley, Nepal Himalayas, 1994 and, Bulletin of Glacier Research, 16, 75–8, 1998.

Fyffe, C. L., Woodget, A. S., Kirkbride, M. P., Deline, P., Westoby, M. J., and Brock, B. W.: Processes at the margins of supraglacial debris
945   cover: quantifying dirty ice ablation and debris redistribution, Earth Surface Processes and Landforms, 2020.

Gardelle, J., Berthier, E., and Arnaud, Y.: Slight mass gain of Karakoram glaciers in the early twenty-first century, Nature geoscience, 5, 322–325, 2012.

Giese, A., Boone, A., Wagnon, P., and Hawley, R.: Incorporating moisture content in surface energy balance modeling of a debris-covered glacier, The Cryosphere, 14, 1555–1577, 2020.

950   Herreid, S. and Pellicciotti, F.: The state of rock debris covering Earth's glaciers, Nature Geoscience, pp. 1–7, 2020.

Heynen, M., Miles, E., Ragettli, S., Buri, P., Immerzeel, W. W., and Pellicciotti, F.: Air temperature variability in a high-elevation Himalayan catchment, Annals of Glaciology, 57, 212–222, 2016.

ICIMOD: AWS Yala Glacier [Data set]. ICIMOD., 2021.

Immerzeel, W. W., Van Beek, L., Konz, M., Shrestha, A., and Bierkens, M.: Hydrological response to climate change in a glacierized
955   catchment in the Himalayas, Climatic change, 110, 721–736, 2012.

Immerzeel, W. W., Kraaijenbrink, P. D., Shea, J., Shrestha, A. B., Pellicciotti, F., Bierkens, M. F., and de Jong, S. M.: High-resolution monitoring of Himalayan glacier dynamics using unmanned aerial vehicles, Remote Sensing of Environment, 150, 93–103, 2014.

Kadel, I., Yamazaki, T., Iwasaki, T., and Abdillah, M. R.: Projection of future monsoon precipitation over the central Himalayas by CMIP5 models under warming scenarios, Climate Research, 75, 1–21, 2018.

960   Kaser, G., Großhauser, M., and Marzeion, B.: Contribution potential of glaciers to water availability in different climate regimes, Proceedings of the National Academy of Sciences, 107, 20 223–20 227, 2010.

Kraaijenbrink, P., Bierkens, M., Lutz, A., and Immerzeel, W.: Impact of a global temperature rise of 1.5 degrees Celsius on Asia's glaciers, Nature, 549, 257–260, 2017.

Kumar, K. K., Rajagopalan, B., Hoerling, M., Bates, G., and Cane, M.: Unraveling the mystery of Indian monsoon failure during El Niño,
965   Science, 314, 115–119, 2006.

Lejeune, Y., Bertrand, J.-M., Wagnon, P., and Morin, S.: A physically based model of the year-round surface energy and mass balance of debris-covered glaciers, Journal of Glaciology, 59, 327–344, 2013.

Liao, H., Liu, Q., Zhong, Y., and Lu, X.: Landsat-based estimation of the glacier surface temperature of Hailuogou glacier, Southeastern Tibetan Plateau, between 1990 and 2018, Remote Sensing, 12, 2105, 2020.

970   Litt, M., Shea, J., Wagnon, P., Steiner, J., Koch, I., Stigter, E., and Immerzeel, W.: Glacier ablation and temperature indexed melt models in the Nepalese Himalaya, Scientific reports, 9, 1–13, 2019.

Mascart, P., Noilhan, J., and Giordani, H.: A modified parameterization of flux-profile relationships in the surface layer using different roughness length values for heat and momentum, Boundary-Layer Meteorology, 72, 331–344, 1995.

Mastrotheodoros, T., Pappas, C., Molnar, P., Burlando, P., Manoli, G., Parajka, J., Rigon, R., Szeles, B., Bottazzi, M., Hadjidoukas, P., et al.: More green and less blue water in the Alps during warmer summers, Nature Climate Change, 10, 155–161, 2020.

Mattson, L. E.: The influence of a debris cover on the mid-summer discharge of Dome Glacier, Canadian Rocky Mountains, IAHS PUBLI-CATION, pp. 25–34, 2000.

Maussion, F., Scherer, D., Mölg, T., Collier, E., Curio, J., and Finkelnburg, R.: Precipitation seasonality and variability over the Tibetan Plateau as resolved by the High Asia Reanalysis, Journal of Climate, 27, 1910–1927, 2014.

McCarthy, M. J.: Quantifying supraglacial debris thickness at local to regional scales, Ph.D. thesis, Scott Polar Research Institute and British Antarctic Survey, 2018.

Miles, E. S., Steiner, J. F., and Brun, F.: Highly variable aerodynamic roughness length (z0) for a hummocky debris-covered glacier, Journal of Geophysical Research: Atmospheres, 122, 8447–8466, 2017.

Mölg, T., Maussion, F., Yang, W., and Scherer, D.: The footprint of Asian monsoon dynamics in the mass and energy balance of a Tibetan glacier, The Cryosphere, 6, 1445, 2012.

Mölg, T., Maussion, F., and Scherer, D.: Mid-latitude westerlies as a driver of glacier variability in monsoonal High Asia, Nature Climate Change, 4, 68–73, 2014.

Moon, S. and Ha, K.-J.: Future changes in monsoon duration and precipitation using CMIP6, npj Climate and Atmospheric Science, 3, 1–7, 2020.

Muñoz Sabater, J.: ERA5-Land monthly averaged data from 1981 to present .Copernicus Climate Change Service (C3S) Climate Data Store (CDS). (Accessed on 01-10-2020), 2019.

Nicholson, L. and Benn, D. I.: Calculating ice melt beneath a debris layer using meteorological data, Journal of Glaciology, 52, 463–470, 2006.

Nicholson, L. and Stiperski, I.: Comparison of turbulent structures and energy fluxes over exposed and debris-covered glacier ice, Journal of Glaciology, 66, 543–555, 2020.

Noilhan, J. and Mahfouf, J.-F.: The ISBA land surface parameterisation scheme, Global and planetary Change, 13, 145–159, 1996.

Östrem, G.: Ice melting under a thin layer of moraine, and the existence of ice cores in moraine ridges, Geografiska Annaler, 41, 228–230, 1959.

Palazzi, E., Filippi, L., and von Hardenberg, J.: Insights into elevation-dependent warming in the Tibetan Plateau-Himalayas from CMIP5 model simulations, Climate Dynamics, 48, 3991–4008, 2017.

Paschalis, A., Fatichi, S., Pappas, C., and Or, D.: Covariation of vegetation and climate constrains present and future T/ET variability, Environmental Research Letters, 13, 104 012, 2018.

Potter, E. R., Orr, A., Willis, I. C., Bannister, D., and Wagnon, P.: Meteorological impacts of a novel debris-covered glacier category in a regional climate model across a Himalayan catchment, Atmospheric Science Letters, p. e1018, 2020.

Quincey, D., Smith, M., Rounce, D., Ross, A., King, O., and Watson, C.: Evaluating morphological estimates of the aerodynamic roughness of debris covered glacier ice, Earth Surface Processes and Landforms, 42, 2541–2553, 2017.

Ragettli, S., Pellicciotti, F., Immerzeel, W. W., Miles, E. S., Petersen, L., Heynen, M., Shea, J. M., Stumm, D., Joshi, S., and Shrestha, A.: Unraveling the hydrology of a Himalayan catchment through integration of high resolution in situ data and remote sensing with an advanced simulation model, Advances in Water Resources, 78, 94–111, 2015.

Ragettli, S., Immerzeel, W. W., and Pellicciotti, F.: Contrasting climate change impact on river flows from high-altitude catchments in the Himalayan and Andes Mountains, Proceedings of the National Academy of Sciences, 113, 9222–9227, 2016.

Reid, T. D. and Brock, B. W.: An energy-balance model for debris-covered glaciers including heat conduction through the debris layer, Journal of Glaciology, 56, 903–916, 2010.

Reznichenko, N., Davies, T., Shulmeister, J., and McSaveney, M.: Effects of debris on ice-surface melting rates: an experimental study, Journal of Glaciology, 56, 384–394, 2010.

Rounce, D., Quincey, D., and McKinney, D.: Debris-covered glacier energy balance model for Imja-Lhotse Shar Glacier in the Everest region of Nepal, 2015.

Rowan, A. V., Nicholson, L. I., Quincey, D. J., Gibson, M. J., Irvine-Fynn, T. D., Watson, C. S., Wagnon, P., Rounce, D. R., Thompson, S. S., Porter, P. R., et al.: Seasonally stable temperature gradients through supraglacial debris in the Everest region of Nepal, Central Himalaya, Journal of Glaciology, pp. 1–12, 2020.

Saha, A. and Ghosh, S.: Can the weakening of Indian Monsoon be attributed to anthropogenic aerosols?, Environmental Research Communications, 1, 061 006, 2019.

Saha, A., Ghosh, S., Sahana, A., and Rao, E.: Failure of CMIP5 climate models in simulating post-1950 decreasing trend of Indian monsoon, Geophysical Research Letters, 41, 7323–7330, 2014.

Sakai, A. and Fujita, K.: Contrasting glacier responses to recent climate change in high-mountain Asia, Scientific reports, 7, 1–8, 2017.

Sakai, A., Fujita, K., and Kubota, J.: Evaporation and percolation effect on melting at debris-covered Lirung Glacier, Nepal Himalayas, 1996, Bulletin of glaciological research, 21, 9–16, 2004.

Sanjay, J., Krishnan, R., Shrestha, A. B., Rajbhandari, R., and Ren, G.-Y.: Downscaled climate change projections for the Hindu Kush Himalayan region using CORDEX South Asia regional climate models, Advances in Climate Change Research, 8, 185–198, 2017.

Scherler, D., Bookhagen, B., and Strecker, M. R.: Hillslope-glacier coupling: The interplay of topography and glacial dynamics in High Asia, Journal of Geophysical Research: Earth Surface, 116, 2011a.

Scherler, D., Bookhagen, B., and Strecker, M. R.: Spatially variable response of Himalayan glaciers to climate change affected by debris cover, Nature geoscience, 4, 156–159, 2011b.

Shah, S. S., Banerjee, A., Nainwal, H. C., and Shankar, R.: Estimation of the total sub-debris ablation from point-scale ablation data on a debris-covered glacier, Journal of Glaciology, 65, 759–769, 2019.

Shaw, T. E., Brock, B. W., Fyffe, C. L., Pellicciotti, F., Rutter, N., and Diotri, F.: Air temperature distribution and energy-balance modelling of a debris-covered glacier, Journal of Glaciology, 62, 185–198, 2016.

Shean, D., Bhushan, S., Montesano, P., Rounce, D., Arendt, A., and Osmanoglu, B.: A systematic, regional assessment of High Mountain Asia Glacier mass balance. Front, Earth Sci, 7, 363, 2020.

Shrestha, R., Kayastha, R., and Kayastha, R.: Effect of debris on seasonal ice melt (2016- 2018) on Ponkar Glacier, Manang, Nepal. Sciences in Cold and Arid Regions, 12 (5): 261- 271. DOI: 10.3724/SP. J. 1226.2020. 00261, Reeju Shrestha et al, pp. 0261–0271, 2020.

Steiner, J. F. and Pellicciotti, F.: Variability of air temperature over a debris-covered glacier in the Nepalese Himalaya, Annals of Glaciology, 57, 295–307, 2016.

Steiner, J. F., Litt, M., Stigter, E. E., Shea, J., Bierkens, M. F., and Immerzeel, W. W.: The importance of turbulent fluxes in the surface energy balance of a debris-covered glacier in the Himalayas, Frontiers in Earth Science, 6, 144, 2018.

Stumm, D., Joshi, S. P., Gurung, T. R., and Silwal, G.: Mass balances of Yala and Rikha Samba Glacier, Nepal from 2000 to 2017, Earth System Science Data Discussions, pp. 1–37, 2020.

Sun, W., Qin, X., Du, W., Liu, W., Liu, Y., Zhang, T., Xu, Y., Zhao, Q., Wu, J., and Ren, J.: Ablation modeling and surface energy budget in the ablation zone of Laohugou glacier No. 12, western Qilian mountains, China, Annals of glaciology, 55, 111–120, 2014.

1050   van den Broeke, M., van As, D., Reijmer, C., and van de Wal, R.: Assessing and improving the quality of unattended radiation observations in Antarctica, Journal of Atmospheric and Oceanic Technology, 21, 1417–1431, 2004.

Verseghy, D. L.: CLASS—A Canadian land surface scheme for GCMs. I. Soil model, International Journal of Climatology, 11, 111–133, 1991.

Vincent, C., Wagnon, P., Shea, J., Immerzeel, W., Kraaijenbrink, P., Shrestha, D., Soruco, A., Arnaud, Y., Brun, F., Berthier, E., et al.:
1055   Reduced melt on debris-covered glaciers: investigations from Changri Nup Glacier, Nepal, 2016.

Wagnon, P.: IACS working group on debris-covered glaciers. AWS North Changri Nup Glacier [Data set]. Hosted on glacioclim.osug.fr., 2021.

Wijngaard, R. R., Steiner, J. F., Kraaijenbrink, P. D., Klug, C., Adhikari, S., Banerjee, A., Pellicciotti, F., Van Beek, L. P., Bierkens, M. F., Lutz, A. F., et al.: Modeling the Response of the Langtang Glacier and the Hintereisferner to a Changing Climate Since the Little Ice Age,
1060   Frontiers in Earth Science, 7, 143, 2019.

Yang, W., Guo, X., Yao, T., Yang, K., Zhao, L., Li, S., and Zhu, M.: Summertime surface energy budget and ablation modeling in the ablation zone of a maritime Tibetan glacier, Journal of Geophysical Research: Atmospheres, 116, 2011.

Yang, W., Yao, T., Zhu, M., and Wang, Y.: Comparison of the meteorology and surface energy fluxes of debris-free and debris-covered glaciers in the southeastern Tibetan Plateau, Journal of Glaciology, 63, 1090–1104, 2017.

1065   Yao, T., Thompson, L., Yang, W., Yu, W., Gao, Y., Guo, X., Yang, X., Duan, K., Zhao, H., Xu, B., et al.: Different glacier status with atmospheric circulations in Tibetan Plateau and surroundings, Nature climate change, 2, 663–667, 2012.

Zhang, Y., Fujita, K., Liu, S., Liu, Q., and Nuimura, T.: Distribution of debris thickness and its effect on ice melt at Hailuogou glacier, southeastern Tibetan Plateau, using in situ surveys and ASTER imagery, Journal of Glaciology, 57, 1147–1157, 2011.

Zhu, M., Yao, T., Yang, W., Xu, B., Wu, G., and Wang, X.: Differences in mass balance behavior for three glaciers from different climatic
1070   regions on the Tibetan Plateau, Climate Dynamics, 50, 3457–3484, 2018.